

An optical lattice with sound

Yudan Guo,^{1,2} Ronen M. Kroeze,^{1,2} Brendan P. Marsh,^{2,3} Sarang Gopalakrishnan,⁴
Jonathan Keeling,⁵ and Benjamin L. Lev^{1,2,3}

¹*Department of Physics, Stanford University, Stanford CA 94305, USA*

²*E. L. Ginzton Laboratory, Stanford University, Stanford, CA 94305, USA*

³*Department of Applied Physics, Stanford University, Stanford CA 94305, USA*

⁴*Department of Physics, The Pennsylvania State University, University Park, PA 16802, USA*

⁵*SUPA, School of Physics and Astronomy, University of St. Andrews, St. Andrews KY16 9SS, United Kingdom*

(Dated: May 3, 2021)

Quantised sound waves—phonons—govern the elastic response of crystalline materials, and also play an integral part in determining their thermodynamic properties and electrical response (e.g., by binding electrons into superconducting Cooper pairs) [1–3]. The physics of lattice phonons and elasticity is absent in simulators of quantum solids constructed of neutral atoms in periodic light potentials: unlike real solids, traditional optical lattices are silent because they are infinitely stiff [4]. Optical-lattice realisations of crystals therefore lack some of the central dynamical degrees of freedom that determine the low-temperature properties of real materials. Here, we create an optical lattice with phonon modes using a Bose-Einstein condensate (BEC) coupled to a confocal optical resonator. Playing the role of an *active* quantum gas microscope, the multimode cavity QED system both images the phonons and induces the crystallisation that supports phonons via short-range, photon-mediated atom-atom interactions. Dynamical susceptibility measurements reveal the phonon dispersion relation, showing that these collective excitations exhibit a sound speed dependent on the BEC-photon coupling strength. Our results pave the way for exploring the rich physics of elasticity in *quantum* solids, ranging from quantum melting transitions [5] to exotic “fractonic” topological defects [6] in the quantum regime.

Ultracold neutral atoms confined in optical lattices have been a fruitful platform for “emulating” the itinerant motion of electrons in crystals [7]. Optical lattices, however, lack a crucial feature of real crystal lattices, which is *elasticity*. Real crystal lattices vibrate, deform in response to electrons, and transmit stresses; in contrast, optical lattices are nondynamical. Elasticity has recently seen a revival of interest, motivated by developments such as “fracton-elasticity duality” [6]. While the motion of ions in real crystals is classical, a natural question is how elasticity would change in the presence of strong quantum zero-point motion of the atoms in the crystal; few controlled experimental studies of this regime exist. We realise a system that combines crystalline elasticity with quantum-degenerate motion, in the form of a compliant optical lattice arising from the crystallisation of Bose-condensed Rb atoms. While mimicking the effect of phonons in static optical lattices has been proposed [8], our method yields a continuum of phonon modes akin to those in solid-state materials.

Crystallisation is the spontaneous breaking of the continuous translational symmetry of space. Due to this symmetry-breaking, a crystal has a manifold of physically distinct equilibrium states, which are related to one another by global translations (i.e., by sliding the entire crystal). Global, zero-momentum ($k = 0$) translations connect these equilibrium states and cost no free energy. Additionally, crystals with *local* interactions have a continuum of finite- k modes with arbitrarily low energies: these modes, called phonons, involve *locally* sliding the crystal by an amount that varies slowly in space with a period $2\pi/k$. Because global translations cost no en-

ergy, while local translations do, a crystal is *rigid*, and responds globally to local stresses. The phonon excitation branch, which is the Goldstone mode of the broken translational symmetry, governs the elastic properties of crystals. The properties of the phonon branch are intimately tied to those of topological defects, such as dislocations, which have recently been identified as “fractonic” excitations. In contrast, for symmetry breaking arising from all-to-all interactions (or other sufficiently long-range interactions), while the $k = 0$ zero mode may remain in place, there is a gap to all $k \neq 0$ excitations. This gives topological defects an *extensive* energy cost, and thus, in these long-range crystals, any nontrivial elastic response is frozen out. (When the atoms forming a crystal are already Bose-condensed, so that the crystal is a “supersolid,” there are additional superfluid Goldstone modes. These superfluid modes are associated with the $U(1)$ phase of the condensate itself and also exist in the absence of a lattice [9, 10]. Sound propagation and diffusion has been studied with strongly interacting fermions [11, 12].)

The primarily contact interactions among Rb do not support crystallisation. Optical cavity photons, however, can mediate interactions that do support crystallisation, as follows. We begin by considering a pump field oriented transverse to a Fabry-Pérot cavity axis that is far detuned from all but a single resonance. Above a critical threshold pump strength, a density wave (DW) polariton condensate forms via a superradiant (Hepp-Lieb-Dicke) phase transition: The N intracavity atoms co-operatively scatter pump photons into the cavity, forming a coherent optical state, while concomitantly the

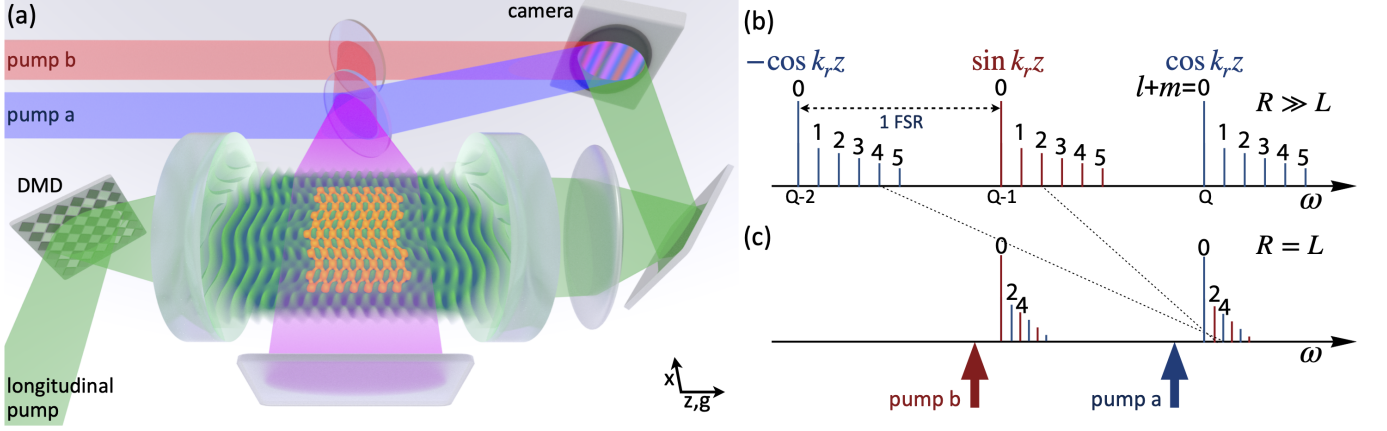


FIG. 1. **Transverse, double-pumped confocal QED system coupled to a BEC.** (a) Sketch of the vibrating atomic density wave (orange) created inside the confocal cavity field (green). Blue and red transverse pump fields are combined (purple) and retroreflected to form a standing wave. A beamsplitter directs some pump light onto a CCD camera to serve as a local oscillator (LO) for the holographic imaging of the spatially dependent phase and amplitude of the cavity emission. A digital micromirror device (DMD) injects patterns of light for measuring dispersion relations: This light longitudinally pumps the cavity along \hat{z} at frequency ω and transverse wavevector k_\perp along \hat{x} . The momentum distribution of the atoms are measured in time-of-flight via absorption imaging along \hat{x} (not shown). (b) Spectrum of a cavity whose radius of curvature R is much greater than its length L , which thus operates in the resolved-mode regime of single or few-mode cavities. Families of modes with fixed longitudinal mode number Q have the same longitudinal phase offset; they differ in phase by $\pm\pi/2$ from families with $Q \pm 1$ one FSR away. (c) The confocal cavity mode spectrum showing even parity families. (Frequency-degenerate transverse modes, labelled by the sum of their indices $l + m$, are dispersed in ω for ease of viewing.) The modes in each family alternate in longitudinal phase. The blue and red arrows indicate the transverse pumps a and b, respectively.

atoms adopt one of two checkerboard configurations of the $\lambda/2$ -period lattice [13, 14]. This $\cos k_r x \cos k_r z$ lattice is formed by the interference of the pump field with the emergent cavity field. The two-photon scattering process excites the $k = 0$ BEC into a superposition of $|k_x, k_z\rangle = |\pm k_r, \pm k_r\rangle$ momentum modes, where \hat{x} (\hat{z}) is the pump (cavity) axis, the pump and cavity fields are of wavelength $\lambda \approx 780$ nm, and $k_r = 2\pi/\lambda \approx 8$ rad/ μm is the recoil momentum; $\hbar\omega_r = \hbar^2 k_r^2 / 2m$ is the recoil energy, approximately 3.8 kHz. The state is stable if the pump frequency ω_P is red-detuned by an amount $\Delta_C = \omega_P - \omega_C < 0$ from the cavity resonance ω_C .

Such single-mode experiments have enabled the exploration of a variety of quantum collective phenomena [15–18], but do not have a continuous translational symmetry and are thus neither rigid nor elastic. A continuous translational symmetry can be restored if one adds a second cavity mode—e.g., by using a ring-cavity geometry [19–21] or crossing two cavities [22, 23]. The free phase between the two cavity fields gives rise to a continuous $U(1)$ family of steady states, which can be related by continuous global displacement of the atoms. (We will explain this mechanism below.) However, since in these experiments the interactions are mediated by finitely many cavity modes, the interactions are infinite-range, so the “crystal” does not allow for nontrivial elastic deformations.

Coupling atoms to far more than two modes is necessary to create a compliant lattice that may, e.g., lead to superfluids with quantum liquid crystalline structure

or exhibiting Meissner-like effects and Peierls instabilities [19, 20, 24, 25]. One can superpose many degenerate modes to form compact supermodes—localised photon wavepackets [17, 26]. Exchanging these localised photons leads to finite-range interactions and momentum exchange [26–28]. As such, when a multimode cavity is combined with a double-pumping scheme to engineer a $U(1)$ symmetry, a fully fledged Goldstone mode with a dispersion relation should emerge. If using a BEC, the result would be a supersolid with phonons. (Phonons have also been proposed, e.g., as elements of composite “refracton” excitations [29, 30] and exist as natural modes in ion traps [31].)

In what follows, we first review how a $U(1)$ symmetry can be engineered by double-pumping in the context of a two-mode cavity [28]; we then extend it to multimode cavities. We consider two pump fields, labelled ‘a’ and ‘b’, each detuned by Δ_C from one of two cavity modes spaced one free spectral range (FSR) apart. Figure 1a sketches a transversely double-pumped cavity, while Fig. 1b shows the spectrum of a cavity whose length L greatly exceeds its mirrors’ radius of curvature R . Each pump induces an interaction between atom pairs. The combined interaction takes the form:

$$U_{\text{total}}^{\text{sm}} \propto U_a^{\text{sm}} \cos k_r z \cos k_r z' + U_b^{\text{sm}} \sin k_r z \sin k_r z', \quad (1)$$

where $U_i^{\text{sm}} = g_0^2 \Omega_i^2 \cos k_r x \cos k_r x' / \Delta_A^2 \Delta_C$ is the interaction strength induced by each pump field of intensity $\propto \Omega_i^2$. The coupling strength of a single atom to the cavity field is g_0 , and the pumps are detuned from the

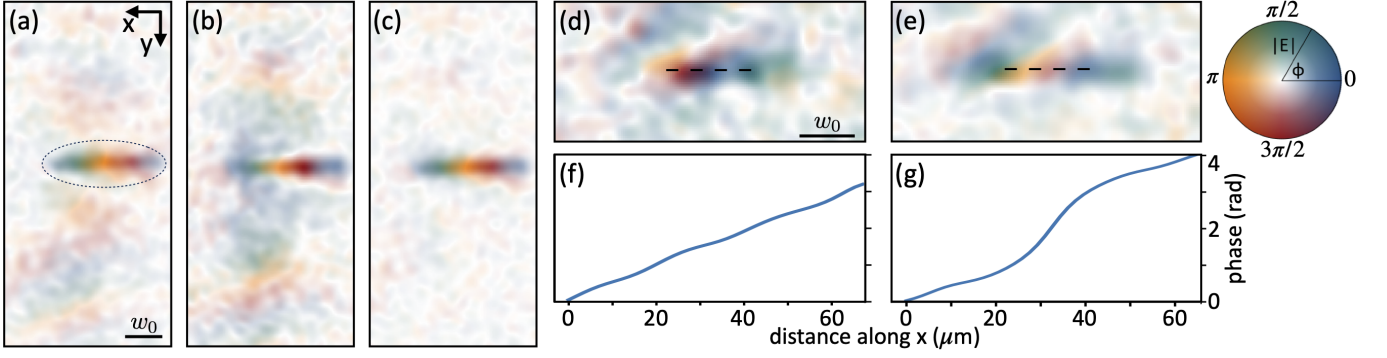


FIG. 2. **Imprinting phonons.** (a-c) We first provide evidence that the nonlocal interaction is cancelled by double-pumping. Holograms of emission from a double-pumped confocal cavity with either (a) the blue pump LO or (b) the red pump LO illuminating the camera. The BEC image appears as the bright rainbow-like stripe. Its position in panel (a) is indicated by the dotted oval. While this emission arises from the local interaction—the first term in Eq. (4)—emission outside this region is due to photons mediating the nonlocal interaction (the second term). (c) The absence of the nonlocal interaction is revealed by taking the digital sum of these holograms. The emission from the nonlocal interaction is absent due to the cancellation of the nonlocal parts in U_a^{mm} and U_b^{mm} when both pumps are present. Colour scale for the field amplitude E and phase ϕ shown at right. (d-g) Evidence for the imprinting of a phonon with $k_\perp = 0.08 \text{ rad}/\mu\text{m} = 1 \times 10^{-2} k_r$. (d,e) Examples of above-threshold cavity emission images taken under the condition of double-pumping (e) with and (d) without the presence of a longitudinal field. The dashed lines show the location and orientation of the line cuts in panels (f) and (g). We observe a full wavelength modulation of the imprinted phonon $\propto e^{ik_\perp x}$, as expected for a BEC stimulated into this specific supermode DW polariton.

atomic level by Δ_A^i , which are much greater than Δ_C and the transition linewidth. The change from cosine to sine reflects the shift by $\lambda/2$ in the longitudinal field profile as the mode's longitudinal index Q changes by one; Q is the number of optical half-wavelengths separating the mirrors. The interaction strengths become equal when $\Omega_a/\Delta_A^a = \Omega_b/\Delta_A^b \equiv \Omega/\Delta_A$, with the result that $U_a^{\text{sm}} = U_b^{\text{sm}} \equiv U^{\text{sm}}$ and the interaction has a continuous translational symmetry along \hat{z} : $U_{\text{total}}^{\text{sm}} = U^{\text{sm}} \cos[k_r(z - z')]$.

To create a lattice where phonons exist, we extend this double-pumping scheme to a multimode cavity of confocal configuration $L = R = 1 \text{ cm}$. Figure 1c shows the confocal mode spectrum, which contains families of degenerate modes of either all-even or all-odd parity [32]. We pump two even mode families spaced one FSR apart. As in the single-mode case, the longitudinal mode profile alternates between cosine and sine. In addition, higher-order transverse modes in the *same* family also alternate in longitudinal profile. The interactions driven by the pumps is therefore $U_{\text{total}}^{\text{mm}} \propto U_a^{\text{mm}} + U_b^{\text{mm}}$, where

$$U_a^{\text{mm}} = U_0 \cos k_r z \cos k_r z' + U_2 \sin k_r z \sin k_r z' \quad (2)$$

$$U_b^{\text{mm}} = U_0 \sin k_r z \sin k_r z' + U_2 \cos k_r z \cos k_r z'. \quad (3)$$

The interaction strengths $U_{0,2}$ are

$$U_{\{0,2\}}/U^{\text{sm}} = \sum_{l,m:l+m=\{0,2\} \bmod 4} \Xi_{l,m}(\mathbf{r}) \Xi_{l,m}(\mathbf{r}') \quad (4)$$

$$= \frac{e^{-\Delta r/\xi}}{\sqrt{\Delta r/\xi}} \pm \cos \left[\frac{\mathbf{r} \cdot \mathbf{r}'}{w_0^2/2} \right]. \quad (5)$$

Here, l, m index the transverse electromagnetic modes $\text{TEM}_{l,m}$ with Hermite-Gaussian mode functions $\Xi_{l,m}(\mathbf{r})$ [26–28]. The waist of the $\text{TEM}_{0,0}$ mode is

$w_0 = 35 \mu\text{m}$. The first term is the local interaction with $\Delta r = |\mathbf{r} - \mathbf{r}'|$ and a minimum range of $\xi \gtrsim 2 \mu\text{m}$; ξ is set by the number of degenerate modes supported by the confocal cavity and Δ_C [26, 33]. The second term is the nonlocal interaction [26, 27]. It cancels in the double-pump scheme, yielding both the desired local interaction and the $U(1)$ translational symmetry:

$$U_{\text{total}}^{\text{mm}} = U^{\text{sm}} \frac{e^{-\Delta r/\xi}}{\sqrt{\Delta r/\xi}} \cos k_r \Delta z. \quad (6)$$

We demonstrate the cancellation of the nonlocal contribution to the cavity-mediated interaction by imaging the phase and amplitude of the above-threshold super-radiant emission under double-pumping; see Supplementary Information for details. Figures 2a,b show the cavity emission from photons mediating U_a^{mm} and U_b^{mm} , respectively. The local interaction created by the atoms gives rise to the image of the BEC in the emergent lattice. That is, the interaction manifests as an emitted image because it is the local light in the cavity that mediates the interaction and this same light leaks out of the cavity [26]; see Supplementary Information. The emission surrounding the BEC is from the nonlocal interaction [27, 28]. This nonlocal interaction is cancelled under double pumping. This manifests as an image without nonlocal emission $\propto U_{\text{total}}^{\text{mm}}$, which we can obtain through the digital summation of the single-LO images. Indeed, this is what we observe in Fig. 2c.

We next demonstrate the imprinting of a phonon above threshold. That is, we cross the supermode DW polariton condensation threshold in the presence of a longitudinal field of fixed wavevector. We then ramp the pump strength to be well above the threshold to obtain the

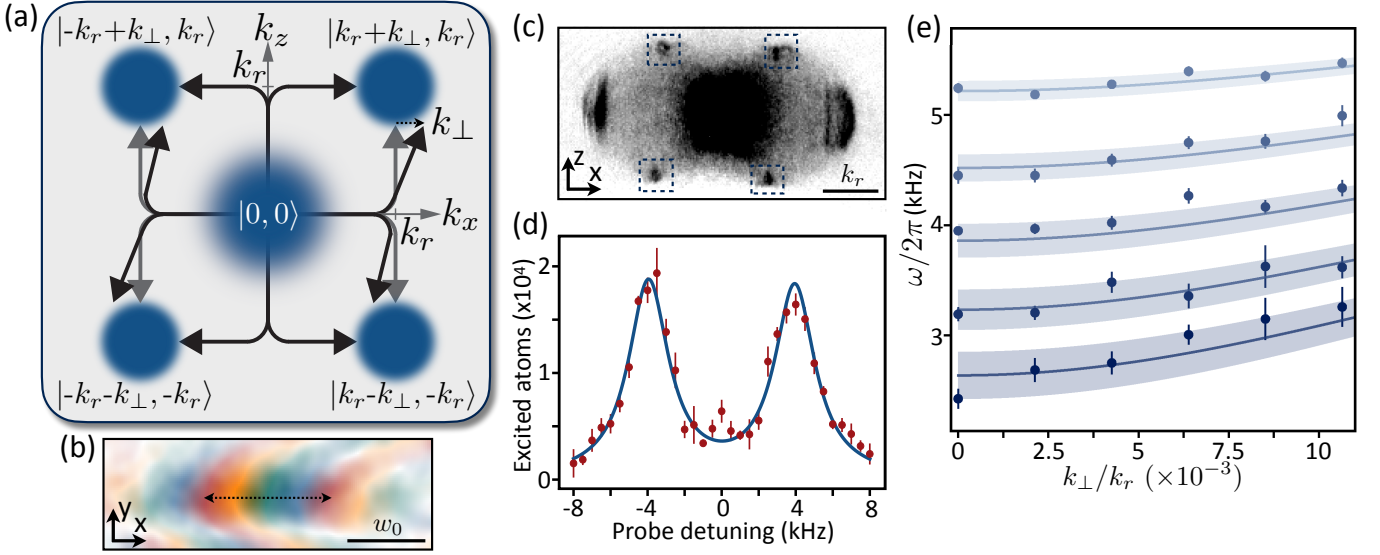


FIG. 3. **Soft-mode dispersion of density-wave polaritons below threshold.** (a) The two-photon scattering process excites atoms by receiving one momentum kick from a pump photon along $\pm\hat{x}$ and another from a cavity photon along $\pm\hat{z}$. The transverse momentum of the higher-order cavity modes shifts the $\pm\hat{x}$ momentum by an amount $\pm k_\perp$. Shown is one possible momentum state; Supplementary Information describes the others. (b) While transversely pumping below threshold, we stimulate a soft mode with a particular k_\perp by seeding the cavity longitudinally. An example of a seed field is shown here, as imaged by the transmission from an empty cavity. Cavity and imaging distortions curve the $k_\perp x$ phase fronts. (c) Below-threshold absorption image of atoms in time-of-flight after a small fraction have been Bragg-stimulated into the four peaks indicated by squares. The other two peaks arise from the pump lattice alone. (d) Example Bragg scattering spectrum showing the number of scattered atoms versus probe detuning from ω_C . Data are the sum of atoms within the squares in panel (c) for $\Omega/\Omega_{\text{th}} = 0.5$ and $k_\perp/k_r \approx 2.5 \times 10^{-3}$. A double Lorentzian (blue curve) is fit to the data, and the excitation energy is half the separation between peaks. Vertical bars represent standard error here and below. (e) Dispersion relation for pump strengths ranging from $\Omega/\Omega_{\text{th}} = 0.3$ at the top (lightest blue) to 0.7 at bottom (darkest blue) in steps of 0.1. Each column of data at fixed k_\perp shows a softening roton mode as the supermode DW polariton condenses at threshold. Data are compared to parameter-free theory curves (with error bands) derived from the theory developed in the Supplementary Information.

emission images in Figs. 2d,e. Like a ferromagnetic transition in the presence of an inhomogeneous longitudinal magnetic field, this breaks the underlying symmetry ‘by hand,’ stimulating the emergent lattice into one particular phonon mode. With no longitudinal field, the cavity emission in Figs. 2d,f reveals a linear background phase gradient, discussed in the Supplementary Information. By contrast, when we imprint a field with a particular k_\perp , we observe the expected phase modulation at $k_\perp x$; see Figs. 2e,g. This constitutes spatial evidence for the driving of a particular vibration mode of the supersolid. It also serves to illustrate the *active* nature of this unusual quantum gas microscope: The cavity fields mediate interactions that support phonons, while their emission provides spatial information about the atomic density profile.

Measuring k -dependent roton softening makes apparent the momentum-exchange arising from the local interaction in the translationally symmetric system. In single-mode cavities, a roton instability at $k = k_r$ results in a DW polariton condensate at threshold [34]. In a confocal cavity, by contrast, the local interaction allows atoms to scatter into a range of states with $|k_\perp|$ added to $|k_r|$ along $\pm\hat{x}$, as illustrated in Fig. 3a. Consequently,

the *supermode* DW polariton shows broad roton minima near k_r . We can probe the dispersion around this point by stimulating the cavity at a particular $k_\perp \geq 0$. This is done by injecting a longitudinal pump field whose amplitude and phase has been programmed by the DMD to be $\propto e^{ik_\perp x}$ [35]; see Fig. 1a for illustration. Figure 3b shows an example field pattern. We can stimulate values close to the characteristic momentum scale of this multimode cavity $\zeta \equiv \xi^{-1} \approx 0.02k_r$; see Supplementary Information.

We measure the dispersion of these k -dependent roton soft modes by cavity-enhanced Bragg stimulation. While pumping below threshold, we stimulate the cavity with the longitudinal probe field at a particular k_\perp set by the DMD. Atoms are more efficiently scattered into the Bragg peaks of Fig. 3a when the frequency and wavevector of the probe field match the roton dispersion, which varies with pump strength Ω . We directly absorption-image these scattered atoms in time-of-flight, as shown in Fig. 3c. Summing the atoms in all four peaks, we can plot the excitation spectrum for a given k_\perp and Ω ; see Fig. 3d. Figure 3e compiles the excitation frequencies. As Ω increases, we see the rotons soften and become more strongly dispersive—i.e., display a stronger k de-

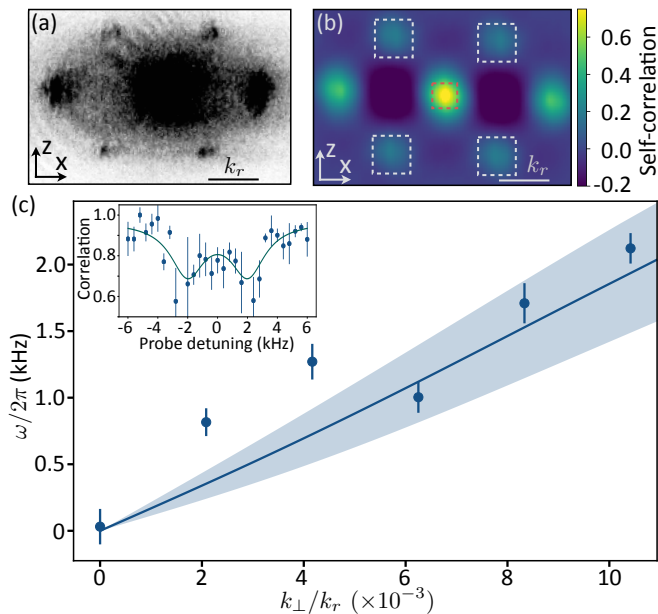


FIG. 4. **Goldstone dispersion relation $\omega(k_\perp)$.** (a) Example above-threshold time-of-flight image recording the momentum distribution $\rho(k)$. (b) The self-correlation analysis yielding $\langle \rho(k + \delta k) \rho(k) \rangle$. The white dashed squares indicate regions of interest for extracting the correlation strength associated with the checkerboard lattice. The correlation strength is calculated by normalising the sum of the values in white squares by that in the central red dashed square. (c) The dispersion relation curve (blue) is overlaid using the theory presented in the Supplemental Information and is parameter-free. The data are consistent with a linear dispersion for $k_\perp \ll \zeta$. The pump strength is $\Omega/\Omega_{\text{th}} = 1.25$. The error band (light blue) represents one-sigma error in the theory parameters. Inset shows an example dynamic susceptibility spectrum obtained from self-correlation analyses taken for $k_\perp/k_r \approx 0.01$. Correlations decrease on resonance because the momentum structure factor differs from the $|0,0\rangle$ state due to the addition of k_\perp .

pendence. At $\Omega \rightarrow 0$, the dispersion is that of atomic DWs set by the atomic mass; with increasing Ω , atomic DWs mix with photons to form DW-polaritons leading to a steeper dispersion; see Supplemental Information.

Finally, we measure the Goldstone dispersion of the phonon modes of the lattice that forms above threshold. We again use cavity-enhanced Bragg stimulation to measure dynamic susceptibility $\omega(k_\perp)$. Above threshold, however, the Bragg peaks of the DW polariton condensate are too populous to discern the additional Bragg-

scattered atoms. Moreover, $k_\perp \ll k_r$ and our maximal time-of-flight is too short to discern the additional $\pm k_\perp$ from the spread in k about the peaks. We instead employ a self-correlation analysis of the momentum distribution to extract the phonon mode resonances; see Supplemental Information. For example, Fig. 4b is the self-correlation of the momentum image in Fig. 4a for a particular ω and k_\perp . The result is the Goldstone mode dispersion curve in Fig. 4c. As derived in the Supplemental Information, the low- k dispersion is linear: $\omega(k_\perp) = v_s |k_\perp|$, with a sound speed $v_s = \sqrt{\hbar\mu/2m + \mu E_I/\zeta^2}$, where the cavity-mediated interaction strength is $E_I = -4\eta^2 N/\Delta_C$ and $\eta = g_0\Omega/4\Delta_A$ is the two-photon coupling. The parameter $\mu \approx E_I - \omega_r$ plays a role analogous to the chemical potential in a weakly interacting dilute Bose gas. One may note that typically $E_I/\zeta^2 \gg \hbar/2m$, so the phonon dispersion is predominantly set by the cavity-mediated interactions. These phonon excitations have a sound velocity of 20 cm/s, $10^4\times$ slower than that in, e.g., copper at room temperature. The theory curve contains no free parameters.

These acoustic phonons are transverse vibrations of the emergent intracavity lattice. In real space, this manifests as a sliding motion of the lattice along the cavity axis \hat{z} propagating along \hat{x} with wavevector \mathbf{k}_\perp , as expected of a transverse mode. The self-consistent cavity optical lattice and atomic DW create a compliant lattice, while individual atoms remain itinerant within the lattice. Adding other atomic spin states or species within this dynamic lattice would more directly mimic electrons in traditional solid-state systems. Replacing the BEC with a degenerate Fermi gas might provide opportunities to study the electron-phonon physics related to polarons [36] in a context complementary to previous studies [37–39] or to study metallic transport in strange metals beyond the semiclassical approximation of long-lived quasiparticles [40]. Moreover, the dual role of itinerant coherent atoms forming a compliant dynamical lattice may also provide access to regimes not attainable in solid-state systems, e.g., to resolve phonon number states in order to perform quantum acousto-optical experiments with supersolids.

We thank Steve Kivelson, Sean Hartnoll, and Vedika Khemani for stimulating discussions. We acknowledge funding support from the Army Research Office. Y.G. and B.M. acknowledge funding from the Stanford Q-FARM Graduate Student Fellowship and the NSF Graduate Research Fellowship, respectively. S.G. acknowledges support from NSF Grant No. DMR-1653271.

-
- [1] C. Kittel, *Introduction to Solid State Physics* (Wiley, 2004).
 - [2] P. M. Chaikin and T. C. Lubensky, *Principles of Condensed Matter Physics* (Cambridge University Press, 1995).
 - [3] M. Tinkham, *Introduction to Superconductivity*, Dover

- Books on Physics (Dover Publications, 2004).
- [4] R. Grimm, M. Weidemüller, and Y. B. Ovchinnikov, in *Advances In Atomic, Molecular, and Optical Physics*, Vol. 42, edited by B. Bederson and H. Walther (Elsevier, 2000) pp. 95–170.
- [5] A. J. Beekman, J. Nissinen, K. Wu, K. Liu, R.-J. Slager,

- Z. Nussinov, V. Cvetkovic, and J. Zaanen, “Dual gauge field theory of quantum liquid crystals in two dimensions,” *Phys. Rep.* **683**, 1 (2017).
- [6] M. Pretko and L. Radzihovsky, “Fracton-Elasticity Duality,” *Phys. Rev. Lett.* **120**, 195301 (2018).
- [7] I. Bloch, J. Dalibard, and W. Zwerger, “Many-body physics with ultracold gases,” *Rev. Mod. Phys.* **80**, 885 (2008).
- [8] D. González-Cuadra, P. R. Grzybowski, A. Dauphin, and M. Lewenstein, “Strongly Correlated Bosons on a Dynamical Lattice,” *Phys. Rev. Lett.* **121**, 090402 (2018).
- [9] D. M. Stamper-Kurn, A. P. Chikkatur, A. Görlitz, S. Inouye, S. Gupta, D. E. Pritchard, and W. Ketterle, “Excitation of Phonons in a Bose-Einstein Condensate by Light Scattering,” *Phys. Rev. Lett.* **83**, 2876 (1999).
- [10] C. Pethick and H. Smith, *Bose-Einstein condensation in dilute gases* (Cambridge University Press, 2002).
- [11] P. B. Patel, Z. Yan, B. Mukherjee, R. J. Fletcher, J. Struck, and M. W. Zwierlein, “Universal sound diffusion in a strongly interacting Fermi gas,” *Science* **370**, 1222 (2020).
- [12] P. T. Brown, D. Mitra, E. Guardado-Sanchez, R. Nourafkan, A. Reymbaut, C.-D. Hébert, S. Bergeron, A.-M. S. Tremblay, J. Kokalj, D. A. Huse, P. Schauf, and W. S. Bakr, “Bad metallic transport in a cold atom Fermi-Hubbard system,” *Science* **363**, 379 (2018).
- [13] P. Kirton, M. M. Roses, J. Keeling, and E. G. Dalla Torre, “Introduction to the Dicke Model: From Equilibrium to Nonequilibrium, and Vice Versa,” *Adv. Quantum Technol.* **2**, 1800043 (2018).
- [14] F. Mivehvar, F. Piazza, T. Donner, and H. Ritsch, “Cavity QED with Quantum Gases: New Paradigms in Many-Body Physics,” (2021), arXiv:2102.04473 [cond-mat.quant-gas].
- [15] J. Klinder, H. Keßler, M. R. Bakhtiari, M. Thorwart, and A. Hemmerich, “Observation of a Superradiant Mott Insulator in the Dicke-Hubbard Model,” *Phys. Rev. Lett.* **115**, 230403 (2015).
- [16] R. Landig, L. Hruby, N. Dogra, M. Landini, R. Mottl, T. Donner, and T. Esslinger, “Quantum phases from competing short- and long-range interactions in an optical lattice,” *Nature* **532**, 476 (2016).
- [17] A. J. Kollár, A. T. Papageorge, V. D. Vaidya, Y. Guo, J. Keeling, and B. L. Lev, “Supermode-density-wave-polariton condensation with a Bose-Einstein condensate in a multimode cavity,” *Nat. Commun.* **8**, 14386 (2017).
- [18] R. M. Kroeze, Y. Guo, and B. L. Lev, “Dynamical Spin-Orbit Coupling of a Quantum Gas,” *Phys. Rev. Lett.* **123**, 160404 (2019).
- [19] S. Gopalakrishnan, B. L. Lev, and P. M. Goldbart, “Emergent crystallinity and frustration with Bose-Einstein condensates in multimode cavities,” *Nat. Phys.* **5**, 845 (2009).
- [20] S. Gopalakrishnan, B. L. Lev, and P. M. Goldbart, “Atom-light crystallization of Bose-Einstein condensates in multimode cavities: Nonequilibrium classical and quantum phase transitions, emergent lattices, supersolidity, and frustration,” *Phys. Rev. A* **82**, 043612 (2010).
- [21] F. Mivehvar, S. Ostermann, F. Piazza, and H. Ritsch, “Driven-Dissipative Supersolid in a Ring Cavity,” *Phys. Rev. Lett.* **120**, 123601 (2018).
- [22] J. Léonard, A. Morales, P. Zupancic, T. Esslinger, and T. Donner, “Supersolid formation in a quantum gas breaking a continuous translational symmetry,” *Nature* **543**, 87 (2017).
- [23] J. Léonard, A. Morales, P. Zupancic, T. Donner, and T. Esslinger, “Monitoring and manipulating Higgs and Goldstone modes in a supersolid quantum gas,” *Science* **358**, 1415 (2017).
- [24] K. E. Ballantine, B. L. Lev, and J. Keeling, “Meissner-like Effect for a Synthetic Gauge Field in Multimode Cavity QED,” *Phys. Rev. Lett.* **118**, 045302 (2017).
- [25] C. Rylands, Y. Guo, B. L. Lev, J. Keeling, and V. Galitski, “Photon-Mediated Peierls Transition of a 1D Gas in a Multimode Optical Cavity,” *Phys. Rev. Lett.* **125**, 010404 (2020).
- [26] V. D. Vaidya, Y. Guo, R. M. Kroeze, K. E. Ballantine, A. J. Kollár, J. Keeling, and B. L. Lev, “Tunable-range, photon-mediated atomic interactions in multimode cavity QED,” *Phys. Rev. X* **8**, 011002 (2017).
- [27] Y. Guo, R. M. Kroeze, V. D. Vaidya, J. Keeling, and B. L. Lev, “Sign-Changing Photon-Mediated Atom Interactions in Multimode Cavity Quantum Electrodynamics,” *Phys. Rev. Lett.* **122**, 193601 (2019).
- [28] Y. Guo, V. D. Vaidya, R. M. Kroeze, R. A. Lunney, B. L. Lev, and J. Keeling, “Emergent and broken symmetries of atomic self-organization arising from Gouy phase shifts in multimode cavity QED,” *Phys. Rev. A* **99**, 053818 (2019).
- [29] M. Lewenstein, A. Kubasiak, J. Larson, C. Menotti, G. Morigi, K. Osterloh, and A. Sanpera, in *AIP Conference Proceedings*, Vol. 869, edited by C. Roos, H. Häffner, and R. Blatt (AIP, 2006) pp. 201–211.
- [30] S. Ostermann, F. Piazza, and H. Ritsch, “Spontaneous Crystallization of Light and Ultracold Atoms,” *Phys. Rev. X* **6**, 021026 (2016).
- [31] C. Monroe, W. Campbell, L.-M. Duan, Z.-X. Gong, A. Gorshkov, P. Hess, R. Islam, K. Kim, N. Linke, G. Pagano, P. Richerme, C. Senko, and N. Yao, “Programmable quantum simulations of spin systems with trapped ions,” *Rev. Mod. Phys.* **93**, 025001 (2021).
- [32] A. E. Siegman, *Lasers* (University Science Books, Sausalito, CA, 1986).
- [33] R. M. Kroeze, B. P. Marsh, Y. Guo, and B. L. Lev, in preparation (2021).
- [34] R. Mottl, F. Brennecke, K. Baumann, R. Landig, T. Donner, and T. Esslinger, “Roton-Type Mode Softening in a Quantum Gas with Cavity-Mediated Long-Range Interactions,” *Science* **336**, 1570 (2012).
- [35] A. T. Papageorge, A. J. Kollár, and B. L. Lev, “Coupling to modes of a near-confocal optical resonator using a digital light modulator,” *Opt. Express* **24**, 11447 (2016).
- [36] J. T. Devreese and A. S. Alexandrov, “Fröhlich polaron and bipolaron: recent developments,” *Rep. Prog. Phys.* **72**, 066501 (2009).
- [37] M.-G. Hu, M. J. Van de Graaff, D. Kedar, J. P. Corson, E. A. Cornell, and D. S. Jin, “Bose Polarons in the Strongly Interacting Regime,” *Phys. Rev. Lett.* **117**, 055301 (2016).
- [38] N. B. Jorgensen, L. Wacker, K. T. Skalmstang, M. M. Parish, J. Levinsen, R. S. Christensen, G. M. Bruun, and J. J. Arlt, “Observation of Attractive and Repulsive Polarons in a Bose-Einstein Condensate,” *Phys. Rev. Lett.* **117**, 055302 (2016).
- [39] Z. Z. Yan, Y. Ni, C. Robens, and M. W. Zwierlein, “Bose polarons near quantum criticality,” *Science* **368**, 190 (2020).

- [40] Y. Werman, S. A. Kivelson, and E. Berg, “Non-quasiparticle transport and resistivity saturation: a view from the large- N limit,” *npj Quant Mater* **2**, 7 (2017).
- [41] A. J. Kollár, A. T. Papageorge, K. Baumann, M. A. Armen, and B. L. Lev, “An adjustable-length cavity and Bose-Einstein condensate apparatus for multimode cavity QED,” *New J. Phys.* **17**, 043012 (2015).
- [42] R. M. Kroeze, Y. Guo, V. D. Vaidya, J. Keeling, and B. L. Lev, “Spinor Self-Ordering of a Quantum Gas in a Cavity,” *Phys. Rev. Lett.* **121**, 163601 (2018).
- [43] M. H. Szymańska, J. Keeling, and P. B. Littlewood, “Nonequilibrium Quantum Condensation in an Incoherently Pumped Dissipative System,” *Phys. Rev. Lett.* **96**, 230602 (2006).
- [44] A. Altland and B. Simons, *Condensed Matter Field Theory* (Cambridge University Press, 2006).
- [45] J. Lang, F. Piazza, and W. Zwerger, “Collective excitations and supersolid behavior of bosonic atoms inside two crossed optical cavities,” *New J. Phys.* **19**, 123027 (2017).
- [46] M. Guo, F. Böttcher, J. Hertkorn, J.-N. Schmidt, M. Wenzel, H. P. Büchler, T. Langen, and T. Pfau, “The low-energy Goldstone mode in a trapped dipolar supersolid,” *Nature* **574**, 386 (2019), 1906.04633.

SUPPLEMENTARY INFORMATION

CONTENTS

References	5
I. BEC preparation	7
II. Cavity, pump lasers, and frequency locks	8
III. Lattice calibration and pump balancing	8
IV. Holographic reconstruction of cavity emission	9
V. Linear phase gradient in Figure 2 images	9
VI. Generation of longitudinal probe with the DMD	9
VII. Bragg spectroscopy and self-correlation analysis	10
VIII. Self-organisation in a double-pumped confocal cavity	11
A. Derivation of equations of motion	12
1. Effective matter-light coupling	12
2. Approximating the cavity Green’s functions	14
3. Dissipative equations of motion	15
B. Dispersion relation and speed of sound	15
1. Below threshold	16
2. Above threshold	17
IX. Derivation of the form of the light profile emitted from the cavity	18
X. Coupling of a longitudinal probe field into the confocal cavity	19
XI. Comparison to other systems	20

I. BEC PREPARATION

Bose-Einstein condensate production proceeds as in Ref. [41]. To shape the BEC for this experiment, we use the same dynamical trap shaping technique as employed in our previous work reported in Ref. [28]. A nearly pure BEC is created in state $|F = 1, m_F = -1\rangle$. A harmonic potential consisting of two crossed beams of wavelength 1064 nm forms a trap of frequencies $(\omega_x, \omega_y, \omega_z) = 2\pi \times [52.6(2), 52.8(2), 91.5(4)]$ Hz. The BEC population is $N = 4.1(3) \times 10^5$ and has Thomas-Fermi radii of $(R_x, R_y, R_z) = [12.3(2), 12.2(2), 7.1(1)]$ μm . Finally, by changing the dither pattern of the trapping beams perpendicular to the pump, the trap shape is adiabatically deformed to produce an elongated gas of 93 μm along the pump direction \hat{x} . A harmonic potential in the other two directions is maintained with similar trap

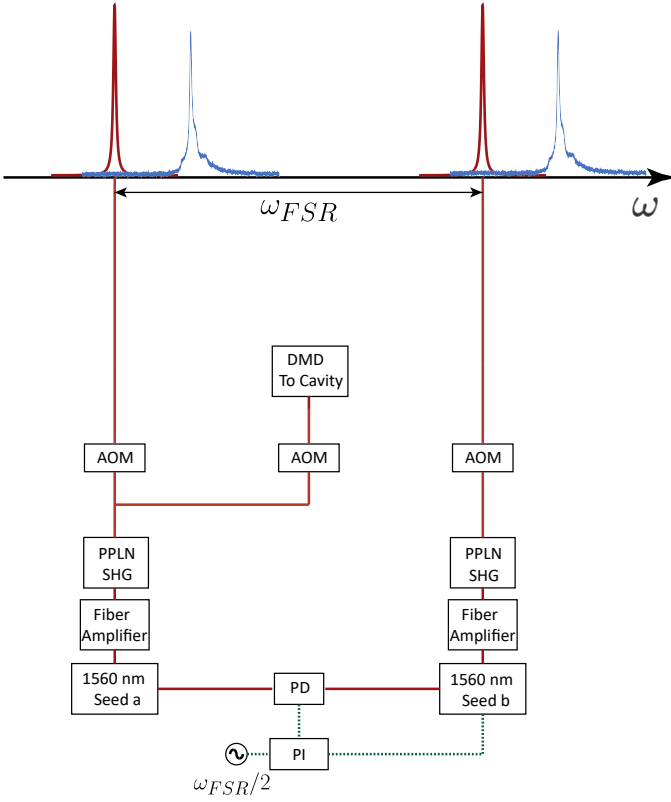


FIG. S1. Pumping and laser locking schematics for two pump fields separated by one free spectral range (FSR). Blue trace is the experimentally measured confocal transmission, while red curve is an illustration of the pump field line shape detuned by Δ_C from the nearby cavity resonance in blue. Listed are a proportional-integral (PI) loop filter, photodetector (PD), periodically poled lithium niobate (PPLN) doubling crystals for second harmonic generation (SHG), acousto-optical modulators (AOMs), and a digital micromirror device (DMD).

frequencies in the other two directions. The centre-of-mass of its density distribution lies at $\mathbf{r}_{\text{cm}} = (49 \mu\text{m}, 35 \mu\text{m})$ along \hat{x} and \hat{y} with respect to the cavity centre.

II. CAVITY, PUMP LASERS, AND FREQUENCY LOCKS

The confocal cavity is vibrationally stabilised using the method presented in Ref. [41]. It is 1-cm long and has a radius of curvature $R = 1$ cm, resulting in a waist of its $\text{TEM}_{0,0}$ mode of $w_0 = 35 \mu\text{m}$. Its finesse is 5.5×10^4 , yielding a cavity linewidth of $\kappa = 137$ kHz. With a single-atom, single-mode coupling g_0 of $2\pi \times 1.47$ MHz, the single-atom, single-mode cooperativity is $C = 2g_0^2/\kappa\gamma = 5$, where the atomic linewidth is $\gamma = 2\pi \times 6$ MHz. Assuming a supermode enhancement factor of ~ 10 (proportional to the inverse local interaction length scale ξ) [26, 33], the supermode single-atom cooperativity is $C^* \approx 50$.

The 780-nm pump beams are each derived from a frequency-doubled 1560-nm fiber amplifier and seed laser; see Fig. S1. The relative frequency between the two 1560-nm seed lasers is stabilised with respect to a frequency source oscillating at half of the cavity free spectral range ~ 7.5 GHz. This frequency difference is controlled using a proportional-integral loop filter with feedback applied to seed ‘b’. A portion of the doubled 780-nm light from seed ‘a’ is used as the illumination beam for the digital micro-mirror device. The DMD reflects this light into the path of the longitudinal cavity injection beam. Acousto-optical modulators are used to stabilise the intensity and adjust the relative detuning between the beams. Additional 1560-nm light from seed ‘a’ is used to stabilise the science cavity using the Pound-Drever-Hall technique. The two pumps are detuned from the $5^2S_{1/2}|2, -2\rangle$ to $5^2P_{3/2}$ transition by 96 GHz and 111 GHz, respectively. Throughout the experiments, the pumps are equally detuned from the relevant cavity resonances by $\Delta_C^a = \Delta_C^b \equiv \Delta_C = -2\pi \times 50$ MHz.

III. LATTICE CALIBRATION AND PUMP BALANCING

We calibrate the lattice depth of pump beams by performing Kapitza-Dirac diffraction of the BEC. The phase of the pump fields at the BEC is controlled by the retroreflection mirror shared by the pump beams. Measuring the lattice depth of the combined pump beams, we adjust the translation stage on which this mirror is mounted to match the phases of the pump lattices at the position of the atoms. We note that the beat length of the two pump lattices

(separated in optical frequency by 15 GHz) is ~ 5 mm, much larger than the atomic cloud size. Therefore, small mechanical fluctuations from the mirror mount will not cause the lattice to become out-of-phase at the atoms. The difference in recoil energy from this difference in frequency is on the order of ~ 0.1 Hz and thus negligible, as is the change in wavelength.

To bring into balance the cavity-mediated interactions induced by each pump, we perform a sequence of single-pump self-organisation experiments. We linearly ramp-up each beam in 5 ms and note the time at which the superradiant threshold is reached. The interaction strength can then be balanced by adjusting the ramp rate such that superradiance on a single FSR occurs at the same time for each beam. This ensures that the Raman coupling rate from each FSR is balanced, i.e., $\Omega_a/\Delta_A^a = \Omega_b/\Delta_A^b$, which then balances the cavity interaction strength for each pump.

IV. HOLOGRAPHIC RECONSTRUCTION OF CAVITY EMISSION

To perform the holographic imaging (spatial heterodyne detection) of the cavity emission, we follow the procedure established in Refs. [27, 42] for a single pump field and extend it to the case of two pumps. Above threshold, the cavity emission has optical frequency content at both ω_a and ω_b (the two pump frequencies), separated by one FSR. To fully reconstruct the cavity electric field, therefore, one must illuminate the camera with two large local oscillator (LO) beams at frequencies ω_a and ω_b at different angles with respect to the propagation direction of the cavity emission. This is illustrated in Fig. 1a. The interference between LO and the cavity emission produces an image with an intensity $I_h(\mathbf{r})$ that may be expressed as

$$I_h(\mathbf{r}) = \sum_{i=a,b} |E_{c,i}(\mathbf{r})|^2 + |E_{LO,i}(\mathbf{r})|^2 + 2\chi_i |E_{c,i}(\mathbf{r})E_{LO,i}(\mathbf{r})| \cos[\Delta\mathbf{k}_i \cdot \mathbf{r} + \Delta\phi_i(\mathbf{r}) + \delta_i], \quad (\text{S1})$$

where we have ignored the fast oscillating term at $\omega_b - \omega_a$, and $E_{c,i}$ and $E_{LO,i}$ are the cavity fields and LO fields for the two FSRs, respectively. Reduction of fringe contrast is characterised by the factor χ_i . The additional phase terms δ_i accounts for the overall phase drift between the LO beams and the cavity emission in each experimental realisation due to technical fluctuations of the apparatus. Because of the angle difference, information from the cavity fields $E_{c,a}$ and $E_{c,b}$ are encoded in spatial wavevectors $\Delta\mathbf{k}_a$ and $\Delta\mathbf{k}_b$, respectively. Assuming the cavity field varies slowly over the spatial scale $2\pi/|\Delta\mathbf{k}_i|$, we may then extract the cavity field amplitudes $|E_{c,i}(\mathbf{r})|$ and phase profiles $\Delta\phi_i(\mathbf{r}) + \delta_i$ by demodulating the image at $\Delta\mathbf{k}_i$.

By using this scheme—an LO at each frequency but at different spatial wavevectors—we take a single spatial heterodyne image that simultaneously allows us to reconstruct the intracavity field for each resonance. The phase of the nonlocal emission should differ by π in the two images and indeed this signal cancels in their digital sum, as shown in Fig. 2c.

V. LINEAR PHASE GRADIENT IN FIGURE 2 IMAGES

The origin of the rainbow-like baseline linear phase gradient seen in the images of the supermode DW polariton is unrelated to the phonon physics presented. It is likely an artefact of a small-angle ($\sim 0.45^\circ$) misalignment between the BEC and \hat{x} (inducing an apparent phase shift) as well as from nonlinear effects due to pumping far above threshold ($\Omega/\Omega_{\text{th}} \approx 20$, in this case). While strong pumping is needed to obtain these illustrative, high signal-to-noise images, it is unnecessary for the phonon dispersion measurements reported in main text. That is, we employ far weaker, near-threshold pump strengths in the experiments reported in Figs. 3 and 4.

We also note that the images in Figs. 2d,e are taken by first exciting the phonon modes near the pump power $\Omega \approx \Omega_{\text{th}}$ and then ramping up one pump to be much stronger than the other for enhanced contrast for the image associated with the LO from that pump. The beam power is rapidly ramped up to $\Omega/\Omega_{\text{th}} \approx 20$ in a duration of 50 μs , which is much faster than the phonon dynamics.

VI. GENERATION OF LONGITUDINAL PROBE WITH THE DMD

The DMD plane is set at approximately the Fourier plane of the cavity centre by using a 100-mm focal length in-vacuum plano-convex lens. The phase aberration of the DMD and misalignment of the illumination beam must be calibrated out of the field images sent into the cavity. We first calibrate these aberrations with an out-of-vacuum setup, similar to that used in Ref. [35]. Then, using a cavity that is far from the confocal degeneracy point, an additional quadratic phase correction is added onto the DMD transfer function to effectively bring the DMD plane

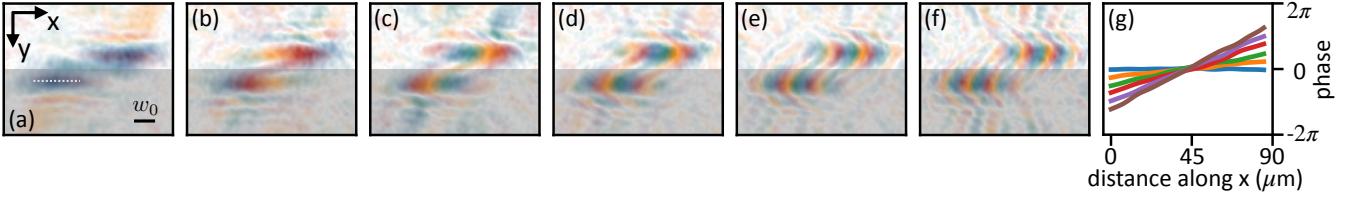


FIG. S2. Measured DMD probe transmission cavity field and their phase profile line cuts. The values of k_{\perp}/k_r in panels (a)–(f) are $[0, 2.1, 4.2, 6.3, 8.5, 10.6] \times 10^{-3}$, respectively. The white dashed line in panel a shows the length of the cuts in panel g. Additional features around the main probe field are due to imperfections of the confocal cavity and stray light from the DMD probe beam. The grey area is the half plane that contains the mirror image of the probe field, and we do not show this redundant portion of the image in the main text figures.

to the Fourier plane of the cavity centre. Finally, any intracavity field we desire can be generated by programming its Fourier transform to be displayed on the DMD. In our experiment, we perform Bragg spectroscopy at six different momenta; the measured DMD probe fields associated with these momenta are shown in Fig. S2. The maximum k_{\perp} modulation we can inject is limited by the numerical aperture of the lens that in-couples the DMD light and by the holding piece of the mirror.

VII. BRAGG SPECTROSCOPY AND SELF-CORRELATION ANALYSIS

The dynamic susceptibility of the system can be measured by using the longitudinal probe imprinted with a phase modulation $\propto k_{\perp}$ along \hat{x} to stimulate, along with the pump fields, the scattering of atoms into the momentum states $|\Psi(k_{\perp})\rangle_{+} = \sum_{\sigma, \tau=\pm 1} |\tau k_r + \sigma k_{\perp}, \sigma k_r\rangle$, as illustrated in Fig. 3a. There is another possible set of states that we do not choose to stimulate or imprint given by $|\Psi(k_{\perp})\rangle_{-} = \sum_{\sigma, \tau=\pm 1} |\tau k_r - \sigma k_{\perp}, \sigma k_r\rangle$; note that $|\Psi(-k_{\perp})\rangle_{+} = |\Psi(k_{\perp})\rangle_{-}$. We choose $|\Psi\rangle_{+}$ versus $|\Psi\rangle_{-}$ by setting the phase of the field imprinted by the DMD. The $|\Psi\rangle_{+}$ state yields the phase *advancing* images in the main text. Because the scattering is coherent, the total atomic state is in a superposition of $|\Psi(k_{\perp})\rangle_{+}$ and $|0, 0\rangle$. In real space, adding the $|\Psi\rangle_{+}$ excitation on top of a uniform checkerboard lattice corresponds to adding a shearing lattice distortion.

We perform Bragg spectroscopy of the system's excitations by monitoring the increase in the population of the scattered atoms in the time-of-flight images versus the relative detuning between the longitudinal probe and the transverse pump. This detuning is adjusted with an AOM on the longitudinal probe beam path. The pump power is first ramped up to prepare the system with a given cavity-mediated interaction strength, and then the longitudinal probe beam is pulsed on for 0.5 ms. For measurements of mode-softening below the transition threshold, the response can be read-out by directly counting the atom population excited into the $|\Psi\rangle_{+}$ momentum state. There are no background atoms at these momenta because there is no population of this momentum state in the normal phase: any atom signal is due to the Bragg excitation. The resonance frequency is extracted by fitting the spectrum to a symmetric double-Lorentzian peak. The set of such frequencies is plotted in Fig. 3e along with curves produced using the theory presented below. The blue uncertainty bands are primarily due to the atom number uncertainty in the cavity-mediated interaction strength. The bands broaden close to threshold where the photon contribution plays an increased role.

For measurements above the threshold, however, the situation is complicated by the macroscopic population of atoms already in the $|\Psi\rangle_0 = \sum_{\sigma, \tau=\pm 1} |\tau k_r, \sigma k_r\rangle$ excited momentum state. While the longitudinal probe creates an additional momentum excitation, the additional atoms are hard to distinguish from that already present because a) the number of these atoms is small compared to the number already condensed into this state, and b) $k_{\perp} \ll k_r$, so that $|\Psi\rangle_{+}$ cannot be distinguished from $|\Psi\rangle_0$ given the limited 20 ms time-of-expansion of the time-of-flight image. Thus, the same momentum-space atom-counting method used for below-threshold spectroscopy measurements is not viable.

We therefore turn to an alternative method that uses these same absorption time-of-flight (TOF) images, but performs an analysis based on momentum correlations rather than momentum-space atom counting. To explain how this works, we first note that in real space, the longitudinal probe creates a small periodic distortion in the originally perfect checkerboard lattice. We can quantify this distortion by computing the momentum-space self-correlation $\langle \rho(\mathbf{k} + \delta \mathbf{k}) \rho(\mathbf{k}) \rangle$ of the atomic momentum distribution $\rho(\mathbf{k})$, which can be computed from $\langle \rho(\mathbf{r} + \delta \mathbf{r}) \rho(\mathbf{r}) \rangle_{\text{TOF}}$ in each TOF image. By focusing on the correlation between the shape of the wavepackets centred at momentum states $|\Psi\rangle_0$ and $|0, 0\rangle$, we can discern the presence of atoms excited to $\pm k_{\perp}$ states. This is because the correlation in the shape of $\rho(\mathbf{k})$ at $\mathbf{k} = (0, 0)$ and at the four $(\pm k_r, \pm k_r)$ regions is strongest when a perfect checkerboard lattice is present: the

wavepacket of the excited momentum state $|\Psi\rangle_0$ is simply a momentum displacement of that at $\mathbf{k} = (0, 0)$. However, in the presence of a small lattice distortion given by k_\perp , the structure factor is reduced and destructive matter-wave interference results in a reduction in the correlation. This correlation reduction is what is plotted in the inset of Fig. 4. The phonon mode resonances are manifest in the correlation signal dips.

To perform the above-threshold measurement, we first fit the entire image to a broad 2D Gaussian profile as an estimate of the background contribution arising from atom heating and from atom scattering halos resulting from the pumps. Then the self-correlation analysis is performed on the background-subtracted images. Due to imperfect subtraction, negative values appear in parts of the correlation. Note that since we are only interested in the correlations between Bragg peaks—all positive valued—the negative values do not affect the results. This analysis is repeated for each value of probe detuning ω and k_\perp to form the experimental $\omega(k_\perp)$ dispersion curve shown in Fig. 4. Due to the sensitivity to atom number fluctuations in the correlation versus ω spectroscopy data, we perform bootstrap sampling to obtain a more reliable error estimate for the data points comprising $\omega(k_\perp)$.

VIII. SELF-ORGANISATION IN A DOUBLE-PUMPED CONFOCAL CAVITY

To derive a theory for obtaining the dispersion-relation curves plotted in the figures of the main text, we start with the Hamiltonian describing atoms coupled to two degenerate resonances of a confocal cavity under the transverse double-pump scheme:

$$\begin{aligned} H = & - \sum_{\mu} \Delta_{\mu} \hat{a}_{\mu}^{\dagger} \hat{a}_{\mu} - \sum_{\mu} \Delta_{\mu} \hat{b}_{\mu}^{\dagger} \hat{b}_{\mu} \\ & + N \int d^3 \mathbf{x} \hat{\Psi}^{\dagger}(\mathbf{x}) \left(-\frac{\nabla^2}{2m} + V(\mathbf{x}) + U |\hat{\Psi}(\mathbf{x})|^2 \right) \hat{\Psi}(\mathbf{x}) \\ & + N \int d^3 \mathbf{x} \hat{\Psi}^{\dagger}(\mathbf{x}) \left(\frac{|\hat{\phi}_a|^2}{\Delta_A^a} + \frac{|\hat{\phi}_b|^2}{\Delta_A^b} \right) \hat{\Psi}(\mathbf{x}), \end{aligned} \quad (\text{S2})$$

where N is the number of atoms and Δ_A^a and Δ_A^b are the atomic detuning of the two pumps. The terms in the first line are the cavity field energies in a frame rotating at one FSR. The terms in the second line are the atomic kinetic energy, potential energy from a trap $V(x)$, and contact interaction of strength U (note this is separate from the cavity mediated atom-atom interaction discussed in the main text). The third line contains the interaction terms between the BEC and the two cavity mode families. The matter wave field is denoted by $\hat{\Psi}(\mathbf{x})$, while the light fields are $\hat{\phi}_a$ and $\hat{\phi}_b$, which contain both the standing-wave transverse pump and a sum over all cavity modes with transverse and longitudinal spatial dependence. In writing the above, we have set $\hbar = 1$, and we will continue to do so throughout this and following sections.

For notational ease, we index the transverse modes with the single variable μ , rather than separate indices l and m for the Hermite-Gauss functions along the \hat{x} and \hat{y} , respectively. We thus use $\mu = \{l, m\}$ to label the transverse electromagnetic mode function $\text{TEM}_{\mu} \equiv \text{TEM}_{l,m}$, and we define the total mode family index $n_{\mu} = l + m$. The light field contains two transverse pumps with strength Ω_a and Ω_b coupled to two degenerate families of cavity modes separated by one FSR. The total fields are

$$\begin{aligned} \hat{\phi}_a(\mathbf{r}) = & \Omega_a \cos(k_r x) \\ & + g_0 \sum_{\mu} \hat{a}_{\mu} \Xi_{\mu}(\mathbf{r}) \cos \left[k_r \left(z + \frac{r^2}{2R(z)} \right) - \theta_{\mu}(z) \right], \\ \hat{\phi}_b(\mathbf{r}) = & \Omega_b \cos(k_r x) \\ & + g_0 \sum_{\mu} \hat{b}_{\mu} \Xi_{\mu}(\mathbf{r}) \cos \left[k_r \left(z + \frac{r^2}{2R(z)} \right) - \theta_{\mu}(z) + \pi/2 \right], \end{aligned} \quad (\text{S3})$$

where $\Xi_{\mu}(\mathbf{r})$ is the spatial profile of a Hermite-Gauss mode of the cavity and the summation runs only over even or odd modes. The form of the light field results in a spatially varying single-photon Rabi frequency $g_0 \Xi_{\mu}(\mathbf{r}) / \Xi_{0,0}(0)$. The radius of curvature is given by $R(z) = z + z_R^2/z$, where z_R is the Rayleigh range. The term $\theta_{\mu}(z)$ accounts for the Gouy phase shift—the fact that in a confocal cavity, different transverse modes, though degenerate, have different

longitudinal phase variation. This is given by

$$\theta_\mu(z) = \vartheta(z) + n_\mu[\vartheta(L/2) + \vartheta(z)] - \Theta, \quad (\text{S4})$$

$$\vartheta(z) = \arctan\left(\frac{z}{z_R}\right). \quad (\text{S5})$$

The phase offset Θ is fixed by the boundary condition that the light field vanishes at the two mirrors. There also is an additional $\pi/2$ phase shift between the two degenerate resonances separated by one cavity FSR; see Ref. [28] for more details.

A. Derivation of equations of motion

1. Effective matter-light coupling

In the main text, we discussed the effective atom-atom interaction mediated by the cavity, specialising to atoms at the cavity midplane, $z = 0$. In this section, we discuss the cavity-mediated interaction more fully. To do this, it is clearer to consider this as an interaction between atomic density waves. We therefore expand the atomic wavefunction as

$$\hat{\Psi} = Z(z - z_0) \left\{ \hat{\psi}_0(\mathbf{r})\mu_0(k_r x) + [\hat{\psi}_1(\mathbf{r})e^{-i(k_r z + \delta)} + \text{H.c.}]\mu_1(k_r x) \right\}, \quad (\text{S6})$$

where $\mu_n(\phi)$ are the 2π periodic eigenfunctions of the Mathieu equation, $\partial_\phi^2 \mu_n + [a_n - 2Q \cos(2\phi)]\mu_n = 0$, with eigenvalues a_n and the $\mu_n(\phi)$ describing wavefunctions in the pump lattice. The dimensionless parameter $Q = -\Omega_a^2/(4\Delta_A^a \omega_r) - \Omega_b^2/(4\Delta_A^b \omega_r)$ is the pump lattice depth in units of the recoil energy $\omega_r = k_r^2/2m$. The factor $Z(z)$ is the envelope function in \hat{z} ; ψ_0 is the condensate wavefunction; ψ_1 is the envelope function of the atomic density wave formed by scattered atoms; and δ is a fixed phase offset that we will later choose for convenience.

Our aim will be to derive coupled equations for the density wave envelope function ψ_1 and the cavity light; this will allow us to find the dispersion of the normal modes (DW polaritons), both below and above the DW polariton condensation threshold. To consider the cavity fields, we may first focus on a single degenerate resonance, and then later combine the effects of both resonances. The linear-order light-matter coupling term in the Hamiltonian is

$$H_{LM}^a = \frac{g_0 \Omega}{\Delta_A^a} \int d^3 \mathbf{x} |\Psi(\mathbf{x})|^2 \sum_\mu \Xi_\mu(\mathbf{r})(\hat{a}_\mu^\dagger + \hat{a}_\mu) \cos(k_r x) \cos[k_r z - \theta_\mu(z)]. \quad (\text{S7})$$

We have assumed that the Rayleigh range is much larger than the BEC, enabling us to drop the $r^2/2R(z)$ term. We next integrate-out the z dependence because the dynamics of interest occur in the transverse plane. This can be done straightforwardly in the limit where we assume $Z(z - z_0)$ has a width w_z and that $\lambda \ll w_z \ll z_R$. The first inequality allows us to drop any terms oscillating at wavevectors k_r or $2k_r$ along \hat{z} ; this imposes momentum conservation so that recoiling atoms receive momentum kicks given by the difference between the pump and cavity momenta. The second condition means that we can evaluate the slowly varying phase terms as being effectively constant over the width of the gas: $\theta_\mu(z) \simeq \theta_\mu(z_0)$. Similarly, we will drop the fast oscillating terms along \hat{x} . Using the expression for the atomic wavefunction in Eq. (S7) and keeping terms up to linear order in $\hat{\psi}_1$, the coupling term then becomes

$$H_{LM}^a = \eta_a \int d\mathbf{r} \sum_\mu \Xi_\mu(\mathbf{r})(\hat{a}_\mu^\dagger + \hat{a}_\mu)[\hat{\psi}_0(\mathbf{r})\hat{\psi}_1^\dagger(\mathbf{r})e^{i(\delta + \theta_\mu(z_0))} + \text{H.c.}], \quad (\text{S8})$$

where $\eta_{a,b} \equiv O(Q)g_0\Omega_{a,b}/4\Delta_A^{a,b}$ is the two-photon coupling strength. The factor $O(Q) = \langle \mu_1(\phi)\mu_0(\phi)\cos(\phi) \rangle$ is the overlap of scattered atoms with the pump potential and the condensate in the pump lattice averaged over one lattice period $\phi \in [0, 2\pi]$. This overlap factor depends on the dimensionless pump lattice strength Q via the form of the Mathieu functions μ_n as defined above. To simplify the expression, we choose $\delta = \Theta - \vartheta(z_0)$ and define $\theta_0 = \pi/4 + \arctan(z_0/z_R)$. We finally arrive at the following form of the interaction

$$H_{LM}^a = \eta_a \int d\mathbf{r} \sum_\mu \Xi_\mu(\mathbf{r})(\hat{a}_\mu^\dagger + \hat{a}_\mu)[\hat{\psi}_0(\mathbf{r})\hat{\psi}_1^\dagger(\mathbf{r})e^{in_\mu\theta_0} + \text{H.c.}]. \quad (\text{S9})$$

The calculation for the degenerate resonance one FSR away (to the red detuning side)—the $\hat{b}_\mu + \hat{b}_\mu^\dagger$ modes—is identical to the above, except there is an additional $\pi/2$ phase shift in θ_μ that shifts the longitudinal cavity profile.

We can now rewrite the full Hamiltonian up to linear order in light-matter coupling as

$$\begin{aligned}
H = & - \sum_{\mu} \Delta_{\mu} \hat{a}_{\mu}^{\dagger} \hat{a}_{\mu} - \sum_{\mu} \Delta_{\mu} \hat{b}_{\mu}^{\dagger} \hat{b}_{\mu} \\
& + \int d\mathbf{r} \hat{\psi}_1^{\dagger}(\mathbf{r}) \left[-\frac{\nabla^2}{2m} + \omega_0 + V(\mathbf{r}) + U|\psi_1(\mathbf{r})|^2 \right] \hat{\psi}_1(\mathbf{r}) \\
& + \eta_a \int d\mathbf{r} \sum_{\mu} \Xi_{\mu}(\mathbf{r}) (\hat{a}_{\mu}^{\dagger} + \hat{a}_{\mu}) [\hat{\psi}_0(\mathbf{r}) \hat{\psi}_1^{\dagger}(\mathbf{r}) e^{in_{\mu}\theta_0} + \text{H.c.}] \\
& + \eta_b \int d\mathbf{r} \sum_{\mu} \Xi_{\mu}(\mathbf{r}) (\hat{b}_{\mu}^{\dagger} + \hat{b}_{\mu}) [i\hat{\psi}_0(\mathbf{r}) \hat{\psi}_1^{\dagger}(\mathbf{r}) e^{in_{\mu}\theta_0} + \text{H.c.}].
\end{aligned} \tag{S10}$$

Here, $\omega_0 = \omega_r[1 + a_1(\mathcal{Q}) - a_0(\mathcal{Q})]$ is the recoil energy of the atoms in the checkerboard momentum state $(\pm k_r, \pm k_r)$ in the presence of a deep pump lattice, written in terms of the Mathieu equation parameter \mathcal{Q} . Note that the additional factor of i in the last line of Eq. (S10) is due to the aforementioned $\pi/2$ shift for \hat{b}_{μ} modes. To model a nonideal degenerate cavity, i.e., one with imperfectly degenerate mode families due to mirror aberrations, we take $\Delta_{\mu} = \Delta_C + n_{\mu}\epsilon$. Here, Δ_C is the pump detuning to the reference mode (typically the peak of the mode spectrum; see, e.g., Fig. S1) and ϵ is the residual mode splitting due to cavity mirror nonidealities; this is typically around 5 MHz for our confocal cavity.

We now focus on the case of two confocal degenerate resonances that contain only the even transverse modes, i.e., $n_{\mu} \bmod 2 = 0$. To account for the infinite number of transverse modes in a more tractable manner, we will find it useful to define the following cavity operators:

$$\begin{aligned}
\hat{\mathcal{A}}(\mathbf{r}) &= \frac{1}{\sqrt{\mathcal{N}_a}} \sum_{\mu} \frac{\Xi_{\mu}(\mathbf{r})}{w_0/\sqrt{2}} \left[\hat{a}_{\mu} \cos(n_{\mu}\theta_0) - \hat{b}_{\mu} \sin(n_{\mu}\theta_0) \right] \mathcal{S}_{\mu}^{+}, \\
\hat{\mathcal{B}}(\mathbf{r}) &= \frac{1}{\sqrt{\mathcal{N}_b}} \sum_{\mu} \frac{\Xi_{\mu}(\mathbf{r})}{w_0/\sqrt{2}} \left[\hat{a}_{\mu} \sin(n_{\mu}\theta_0) + \hat{b}_{\mu} \cos(n_{\mu}\theta_0) \right] \mathcal{S}_{\mu}^{+},
\end{aligned} \tag{S11}$$

where $\mathcal{N}_{a,b}$ are normalisation factors to guarantee bosonic commutation relations and the factor

$$\mathcal{S}_{\mu}^{+} = \frac{1}{2}[1 + (-1)^{n_{\mu}}] \tag{S12}$$

is chosen to cancel the odd modes in a degenerate confocal resonance such that the summation can be carried over all transverse modes. Computing the commutation relations, we find that

$$\begin{aligned}
[\hat{\mathcal{A}}(\mathbf{r}), \hat{\mathcal{A}}^{\dagger}(\mathbf{r}')] &= \frac{1}{\mathcal{N}_a} \sum_{\mu} \frac{\Xi_{\mu}(\mathbf{r})}{w_0/\sqrt{2}} \frac{\Xi_{\mu}(\mathbf{r}')}{w_0/\sqrt{2}} \mathcal{S}_{\mu}^{+} = \frac{1}{2\mathcal{N}_a} [\delta(\mathbf{r} - \mathbf{r}') + \delta(\mathbf{r} + \mathbf{r}')], \\
[\hat{\mathcal{B}}(\mathbf{r}), \hat{\mathcal{B}}^{\dagger}(\mathbf{r}')] &= \frac{1}{\mathcal{N}_b} \sum_{\mu} \frac{\Xi_{\mu}(\mathbf{r})}{w_0/\sqrt{2}} \frac{\Xi_{\mu}(\mathbf{r}')}{w_0/\sqrt{2}} \mathcal{S}_{\mu}^{+} = \frac{1}{2\mathcal{N}_b} [\delta(\mathbf{r} - \mathbf{r}') + \delta(\mathbf{r} + \mathbf{r}')],
\end{aligned} \tag{S13}$$

where the normalisation condition of the Hermite-Gauss mode function is given by

$$\int \frac{d\mathbf{r}}{w_0^2/2} \Xi_{\mu}(\mathbf{r}) \Xi_{\mu}(\mathbf{r}) = 1. \tag{S14}$$

The appearance of the mirror-image term $\delta(\mathbf{r} + \mathbf{r}')$ is due to the fact that the summation is restricted to all modes with even spatial symmetry. We note that this term does not play a role in the atom-cavity interaction because we place the BEC away from the cavity centre so that no atoms exist at the mirror image position. Consequently, the same normalisation $\mathcal{N}_{a,b} = 1/2$ satisfies the bosonic commutation relation for both $\hat{\mathcal{A}}$ and $\hat{\mathcal{B}}$. Using orthonormality of the Hermite-Gauss mode functions Ξ_{μ} , the original boson modes may be rewritten as

$$\begin{aligned}
\hat{a}_{\mu} &= \sqrt{\frac{1}{2}} \int d\mathbf{r} \frac{\Xi_{\mu}(\mathbf{r})}{w_0/\sqrt{2}} \left[\hat{\mathcal{A}}(\mathbf{r}) \cos(n_{\mu}\theta_0) + \hat{\mathcal{B}}(\mathbf{r}) \sin(n_{\mu}\theta_0) \right], \\
\hat{b}_{\mu} &= \sqrt{\frac{1}{2}} \int d\mathbf{r} \frac{\Xi_{\mu}(\mathbf{r})}{w_0/\sqrt{2}} \left[\hat{\mathcal{A}}(\mathbf{r}) \cos(n_{\mu}\theta_0) - \hat{\mathcal{B}}(\mathbf{r}) \sin(n_{\mu}\theta_0) \right].
\end{aligned} \tag{S15}$$

Employing the $\hat{\mathcal{A}}, \hat{\mathcal{B}}$ basis, we can now rewrite the original Hamiltonian in terms of an inverse Green's function $\mathcal{D}^{-1}(\mathbf{r}, \mathbf{r}')$:

$$\begin{aligned} H = & -\Delta_C \int \frac{d\mathbf{r}d\mathbf{r}'}{w_0^2/2} [\hat{\mathcal{A}}^\dagger(\mathbf{r})\mathcal{D}^{-1}(\mathbf{r}, \mathbf{r}')\hat{\mathcal{A}}(\mathbf{r}') + \hat{\mathcal{B}}^\dagger(\mathbf{r})\mathcal{D}^{-1}(\mathbf{r}, \mathbf{r}')\hat{\mathcal{B}}(\mathbf{r}')] \\ & + \int d\mathbf{r} \hat{\psi}_1^\dagger(\mathbf{r}) \left[-\frac{\nabla^2}{2m} + \omega_0 + V(\mathbf{r}) + U|\psi_1(\mathbf{r})|^2 \right] \hat{\psi}_1(\mathbf{r}) \\ & + \eta_a \int d\mathbf{r} \frac{w_0}{\sqrt{2}} [\hat{\psi}_1^\dagger(\mathbf{r}) + \hat{\psi}_1(\mathbf{r})][\hat{\mathcal{A}}^\dagger(\mathbf{r}) + \hat{\mathcal{A}}(\mathbf{r})]\psi_0(\mathbf{r}) + \eta_b \int d\mathbf{r} \frac{w_0}{\sqrt{2}} [i\hat{\psi}_1^\dagger(\mathbf{r}) - i\hat{\psi}_1(\mathbf{r})][\hat{\mathcal{B}}^\dagger(\mathbf{r}) + \hat{\mathcal{B}}(\mathbf{r})]\psi_0(\mathbf{r}), \end{aligned} \quad (\text{S16})$$

where

$$\mathcal{D}^{-1}(\mathbf{r}, \mathbf{r}') = \sum_{\mu} (1 + n_{\mu}\tilde{\epsilon})\Xi_{\mu}(\mathbf{r})\Xi_{\mu}(\mathbf{r}'), \quad (\text{S17})$$

and $\tilde{\epsilon} \equiv \epsilon/\Delta_C$. Here, the summation is over all transverse modes with both even and odd spatial symmetry since we have dropped the mirror-image term in the commutation relation for the cavity field operators $\hat{\mathcal{A}}$ and $\hat{\mathcal{B}}$.

2. Approximating the cavity Green's functions

Equation (S16), along with the definition of $\mathcal{D}^{-1}(\mathbf{r}, \mathbf{r}')$, provides a general description of the cavity tuned near to a confocal point, but with some nonzero ϵ . Modelling the dynamics of this is however hard in general, as $\mathcal{D}(\mathbf{r}, \mathbf{r}')$ is not translationally invariant. However, we can approximate this by a translationally invariant function, allowing one to use a momentum space description to find the DW polariton dispersion.

The cavity Green's function can be written as

$$\mathcal{D}(\mathbf{r}, \mathbf{r}') \equiv \sum_{\mu} \frac{\Xi_{\mu}(\mathbf{r})\Xi_{\mu}(\mathbf{r}')}{1 + n_{\mu}\tilde{\epsilon}} = \int d\lambda e^{-\lambda} G(\mathbf{r}, \mathbf{r}', \tilde{\epsilon}\lambda),$$

where we have used

$$G(\mathbf{r}, \mathbf{r}', \varphi) \equiv \sum_{\mu} \Xi_{\mu}(\mathbf{r})\Xi_{\mu}(\mathbf{r}')e^{-n_{\mu}\varphi} = \frac{e^{\varphi}}{2\pi \sinh(\varphi)} \exp \left[-\frac{(\mathbf{r} - \mathbf{r}')^2/w_0^2}{2 \tanh(\varphi/2)} - \frac{(\mathbf{r} + \mathbf{r}')^2/w_0^2}{2 \coth(\varphi/2)} \right]. \quad (\text{S18})$$

This then gives [26]

$$\mathcal{D}(\mathbf{r}, \mathbf{r}') = \frac{1}{2\pi\tilde{\epsilon}} K_0 \left(\frac{2}{\sqrt{\tilde{\epsilon}}} \left| \frac{\mathbf{r} - \mathbf{r}'}{w_0} \right| \sqrt{1 + \frac{\tilde{\epsilon}}{4} \left(\frac{\mathbf{r} + \mathbf{r}'}{w_0} \right)^2} \right), \quad (\text{S19})$$

where K_0 is the modified Bessel function of the second kind. We assume that the spatial extent of $\psi_0(\mathbf{r})$ is smaller than $2w_0/\sqrt{\tilde{\epsilon}} \approx 220 \mu\text{m}$, which is true for our condensate length of $\sim 93 \mu\text{m}$. These assumptions allow us to make the following approximation:

$$\begin{aligned} \mathcal{D}(\mathbf{r}, \mathbf{r}') & \approx \frac{1}{2\pi\tilde{\epsilon}} K_0 \left(\frac{2}{\sqrt{\tilde{\epsilon}}} \left| \frac{\mathbf{r} - \mathbf{r}'}{w_0} \right| \sqrt{1 + \tilde{\epsilon} \left(\frac{\mathbf{r}_{\text{cm}}}{w_0} \right)^2} \right), \\ & \equiv K(|\mathbf{r} - \mathbf{r}'|/\xi), \end{aligned} \quad (\text{S20})$$

where again, $\mathbf{r}_{\text{cm}} = (49 \mu\text{m}, 35 \mu\text{m})$ is the centre of mass coordinate of the gas and

$$\xi \equiv \frac{w_0\sqrt{\tilde{\epsilon}}}{2\sqrt{1 + \tilde{\epsilon}(\mathbf{r}_{\text{cm}}/w_0)^2}}. \quad (\text{S21})$$

Thus, we see that the cavity Green's function is translationally invariant in the limit of $\tilde{\epsilon} \ll 1$. In the limit that $\sqrt{\tilde{\epsilon}}r_{\text{cm}}/w_0 \ll 1$, we have that $\xi \approx w_0\sqrt{\tilde{\epsilon}}/2$. For our system, this local interaction range is 5-6 μm at the Δ_C employed for the spectroscopy data taken here [26, 33].

From the form of Eq. (S20), we find that the approximate Green's function is diagonal in momentum space:

$$\mathcal{D}(\mathbf{k}) = \frac{1}{1 + k^2/\zeta^2}, \quad (\text{S22})$$

where $\zeta = 1/\xi$ is the characteristic momentum scale. Therefore, the dispersion of the cavity field $\hat{\mathcal{A}}, \hat{\mathcal{B}}$ in the small- $\tilde{\epsilon}$ limit is

$$\mathcal{D}^{-1}(\mathbf{k}) = 1 + k^2/\zeta^2. \quad (\text{S23})$$

We note that the well-defined nature of the momentum peaks evident in our spectroscopy experiments—indicating that momentum is a good quantum number—support the assumptions made above.

3. Dissipative equations of motion

Using the above translational invariance, we can now write the mean-field equations of motion for the cavity modes and atoms:

$$\begin{aligned} i\partial_t \psi_1 &= \left[\omega_0 - \frac{\nabla^2}{2m} \right] \psi_1 + \eta \psi_0 [(\mathcal{A}^* + \mathcal{A}) + i(\mathcal{B}^* + \mathcal{B})] \frac{w_0}{\sqrt{2}} + U|\psi_1|^2 \psi_1, \\ i\partial_t \mathcal{A} &= -\Delta_C \left(1 - \frac{\nabla^2}{\zeta^2} \right) \mathcal{A} + \eta \psi_0 (\psi_1^* + \psi_1) \frac{w_0}{\sqrt{2}} - i\kappa \mathcal{A}, \\ i\partial_t \mathcal{B} &= -\Delta_C \left(1 - \frac{\nabla^2}{\zeta^2} \right) \mathcal{B} + i\eta \psi_0 (\psi_1^* - \psi_1) \frac{w_0}{\sqrt{2}} - i\kappa \mathcal{B}. \end{aligned} \quad (\text{S24})$$

Here, $\eta \equiv \eta_a = \eta_b$ is the balanced pump power. We note that \mathcal{A} and \mathcal{B} couple to the real and imaginary part of ψ_1 , respectively.

These equations support two steady-state conditions. There is always a steady state with $\psi_1 = \mathcal{A} = \mathcal{B} = 0$, corresponding to the normal state, below threshold. In addition, above a critical pumping strength a DW polariton condensate state exists. Using the uniform state as an ansatz and choosing the phase of the atom field ψ_1 to be zero, the DW polariton condensate stationary state is given by:

$$\psi_{1S} = \sqrt{\frac{\mu}{U}}, \quad \mathcal{A}_S = \frac{2\eta\sqrt{N}\psi_{1S}}{\Delta_C + i\kappa}, \quad \mathcal{B}_S = 0. \quad (\text{S25})$$

We have introduced μ which plays a role analogous to the chemical potential in a weakly interacting Bose gas and $N = |\psi_0|^2 w_0^2/2$. The steady state condition requires:

$$\mu = -\frac{4\eta^2 N \Delta_C}{\Delta_C^2 + \kappa^2} - \omega_0. \quad (\text{S26})$$

Note that the pump is red-detuned from the cavity resonance and thus $\Delta_C < 0$. The DW polariton condensate state exists only when $\mu > 0$, which requires a sufficiently large pump strength η . We recover the below-threshold state if we set $\mu = 0$.

B. Dispersion relation and speed of sound

To derive the dispersion relation, we now expand around the stationary state by using the Bogoliubov–de Gennes parametrisation, considering a fluctuation with wavevector \mathbf{k} and (complex) frequency ν . Note that in our system, since we are considering ψ_1 as the envelope function of a density wave, $\mathbf{k} \cdot \hat{x} = k_\perp$, $\mathbf{k} \cdot \hat{y} = k_y$, and $\mathbf{k} \cdot \hat{z} = 0$:

$$\begin{aligned} \psi_1(\mathbf{r}, t) &= \psi_{1S} + u e^{-i(\mathbf{k} \cdot \mathbf{r} + \nu t)} + v^* e^{i(\mathbf{k} \cdot \mathbf{r} + \nu^* t)}, \\ \mathcal{A}(\mathbf{r}, t) &= \mathcal{A}_S + c e^{-i(\mathbf{k} \cdot \mathbf{r} + \nu t)} + d^* e^{i(\mathbf{k} \cdot \mathbf{r} + \nu^* t)}, \\ \mathcal{B}(\mathbf{r}, t) &= \mathcal{B}_S + f e^{-i(\mathbf{k} \cdot \mathbf{r} + \nu t)} + g^* e^{i(\mathbf{k} \cdot \mathbf{r} + \nu^* t)}. \end{aligned} \quad (\text{S27})$$

We seek to find how the allowed value(s) of ν depend on \mathbf{k} . Inserting these into the equations of motion, keeping terms up to linear order in small fluctuations, and matching the Fourier components, the equations for the Bogoliubov–de Gennes coefficients are

$$\begin{aligned}
\nu u &= \left[\omega_0 + \frac{k^2}{2m} + 2U\psi_S^2 \right] u + U\psi_S^2 v + \eta\sqrt{N}[c + d + i(f + g)], \\
\nu v &= - \left[\omega_0 + \frac{k^2}{2m} + 2U\psi_S^2 \right] v - U\psi_S^2 u - \eta\sqrt{N}[c + d - i(f + g)], \\
\nu c &= \left[-\Delta_C \left(1 + \frac{k^2}{\zeta^2} \right) - i\kappa \right] c + \eta\sqrt{N}(u + v), \\
\nu d &= - \left[-\Delta_C \left(1 + \frac{k^2}{\zeta^2} \right) + i\kappa \right] d - \eta\sqrt{N}(u + v), \\
\nu f &= \left[-\Delta_C \left(1 + \frac{k^2}{\zeta^2} \right) - i\kappa \right] f - i\eta\sqrt{N}(u - v), \\
\nu g &= - \left[-\Delta_C \left(1 + \frac{k^2}{\zeta^2} \right) + i\kappa \right] g - i\eta\sqrt{N}(v - u).
\end{aligned} \tag{S28}$$

The cavity field fluctuations c, d, f, g can be eliminated by expressing them in terms of the atomic wavefunctions u and v , and then substituting them back into the first two equations. The results are

$$\begin{aligned}
\nu u &= \left(\omega_0 + \frac{k^2}{2m} + 2\mu \right) u + \mu v + \eta^2 N \frac{4\Delta_k u}{(\nu + i\kappa)^2 - \Delta_k^2}, \\
\nu v &= - \left(\omega_0 + \frac{k^2}{2m} + 2\mu \right) v - \mu u - \eta^2 N \frac{4\Delta_k v}{(\nu + i\kappa)^2 - \Delta_k^2},
\end{aligned} \tag{S29}$$

where $\Delta_k \equiv -\Delta_C(1 + k^2/\zeta^2)$. These equations can be re-arranged into the simple form

$$\begin{bmatrix} A(\nu) - \nu & \mu \\ \mu & A(\nu) + \nu \end{bmatrix} \begin{bmatrix} u \\ v \end{bmatrix} = 0, \tag{S30}$$

where

$$A(\nu) \equiv \omega_0 + \frac{k^2}{2m} + 2\mu + \eta^2 N \frac{4\Delta_k}{(\nu + i\kappa)^2 - \Delta_k^2}. \tag{S31}$$

1. Below threshold

Below threshold, as noted above, we set $\mu = 0$. In this case there is no mixing of u and v , and the excitation spectrum can be found from solutions of the equation:

$$\nu = \omega_0 + \frac{k^2}{2m} + \eta^2 N \frac{4\Delta_k}{(\nu + i\kappa)^2 - \Delta_k^2}. \tag{S32}$$

This expression is the dispersion of DW polaritons: the normal-mode frequencies result from mixing the atomic density wave dispersion $k^2/2m$ with the photon-mediated interaction. Focusing on the experimentally relevant limit $\nu, \kappa \ll |\Delta_C|$, we obtain the simple expression

$$\nu(\mathbf{k}) = \omega_0 + \frac{k^2}{2m} + \frac{4\eta^2 N}{\Delta_C(1 + k^2/\zeta^2)}. \tag{S33}$$

As observed in the main text, this expression exhibits a relatively flat dispersion (controlled by the atomic mass) when $\eta = 0$. Because $\Delta_C < 0$, increasing η both softens the mode—reduces $\nu(\mathbf{k} = 0)$ —and leads to a steeper dispersion, due to the \mathbf{k} -dependence of the second, cavity-mediated term. When $4\eta^2 N = -\Delta_C\omega_0$, one has $\nu(\mathbf{k} = 0) = 0$; this corresponds to the point at which the mode becomes entirely soft, and DW polariton condensation occurs. (Note, this condition assumes $\kappa \ll |\Delta_C|$, as introduced above).

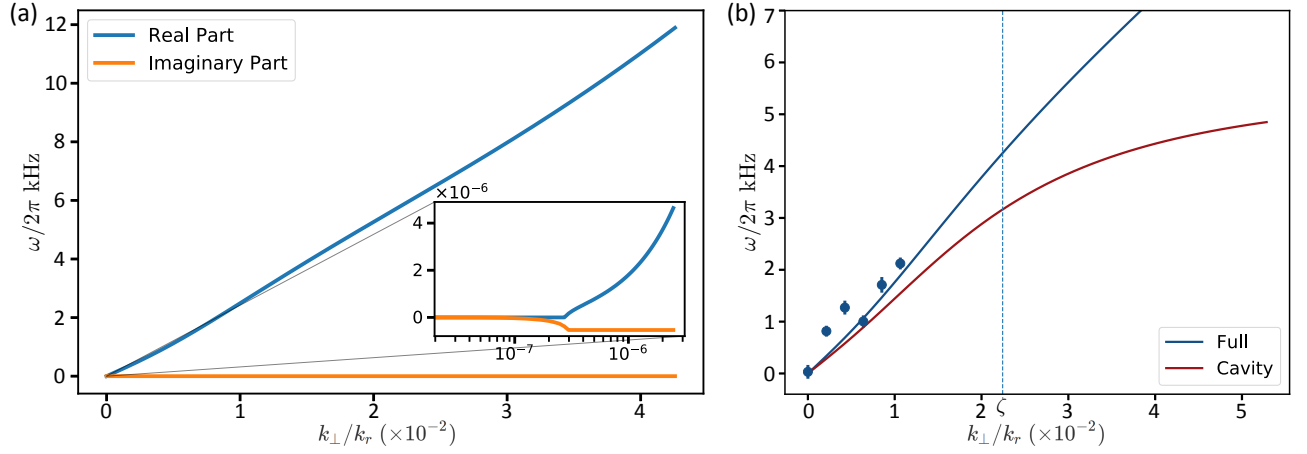


FIG. S3. (a) Numerical solution to the dispersion above threshold. Inset shows the spectrum at small momenta. (b) Full dispersion (blue) contrasted with the cavity-only contribution to the dispersion (red) that does not contain the atomic $k^2/2m$ dispersion. At low momenta, the dispersion is dominated by the cavity contribution. The dashed line shows $k_\perp = \zeta$. The cavity dispersion flattens toward a Debye frequency of ~ 5 kHz at large k_\perp .

2. Above threshold

Above threshold, the frequencies are solutions of the determinant equation:

$$\mu^2 = [A(\nu) - \nu][A(\nu) + \nu]. \quad (\text{S34})$$

To obtain a simple expression, we expand $A(\nu)$ up to linear order in $\nu/|\Delta_k|$ and $\kappa/|\Delta_k|$, which is the relevant limit for the long-wavelength, low-energy regime we explore:

$$A(\nu) = \omega_0 + \frac{k^2}{2m} + 2\mu - \frac{4\eta^2 N}{\Delta_k} \left[1 + \frac{2i\nu\kappa}{\Delta_k^2} \right] + O\left(\left|\frac{\nu}{\Delta_k}\right|^2, \left|\frac{\kappa}{\Delta_k}\right|^2\right). \quad (\text{S35})$$

The determinantal equation for ν in Eq. (S34) can then be solved:

$$\nu(\mathbf{k}) = i\frac{\Gamma_k}{2} \pm \sqrt{(\mathcal{E}_k^2 - \mu^2) - \frac{\Gamma_k^2}{4}}, \quad (\text{S36})$$

where

$$\Gamma_k = -\frac{16N\mathcal{E}_k\eta^2\kappa}{\Delta_k^3}, \quad \mathcal{E}_k = \omega_0 + \frac{k^2}{2m} + 2\mu - \frac{4\eta^2 N}{\Delta_k}. \quad (\text{S37})$$

The Γ_k expression is the excitation gap due to cavity loss. Note that for consistency, the chemical potential μ in this expression should also be expanded up to linear order in $\kappa/|\Delta_C|$ as

$$\mu = -\frac{4\eta^2 N}{\Delta_C} - \omega_0, \quad (\text{S38})$$

so that $\mathcal{E}_0 = \mu$ (recalling that $\Delta_{k=0} = -\Delta_C$).

Because $\kappa \ll |\Delta_C|$, the dissipative term Γ_k has a small effect except at very small k . Outside this small k regime, the real part of the dispersion can be expanded up to linear order to yield the dispersion relation of the acoustic photon mode:

$$\text{Re}[\nu(\mathbf{k})] \simeq \sqrt{2\mu(\mathcal{E}_k - \mu)} = v_s |\mathbf{k}|, \quad (\text{S39})$$

where the speed of sound takes the form

$$v_s = \sqrt{\mu \left(\frac{1}{2m} + \frac{E_I}{\zeta^2} \right)}, \quad (\text{S40})$$

in terms of the cavity-mediated interaction energy scale $E_I = -4N\eta^2/\Delta_C$. One may note that $E_I/\zeta^2 \gg 1/2m$, so the sound velocity is principally determined by the cavity-mediated interaction strength. For the above-threshold data presented in the main text, $v_s \approx 0.16$ m/s.

Using the above expression, we can also describe the diffusive regime that occurs at very small momenta. We use that $\mathcal{E}_k^2 - \mu^2 \simeq v_s^2 k^2$ at small momentum to find that as $\mathbf{k} \rightarrow 0$ the gapless branch of $\nu(\mathbf{k})$ has the purely imaginary diffusive spectrum $\nu(\mathbf{k}) = i2v_s^2 k^2/\Gamma_k$, as also found for microcavity polariton condensates [43]. This crosses over to the linear sound dispersion when $v_s k = \Gamma_k/2$. Figure S3 plots the numerical solution to the above-threshold determinant equation using experimental parameters. The imaginary part contribution $\propto \Gamma_k$ is indeed negligible.

As discussed above, one should note that k_\perp is measured from the $(\pm k_r, \pm k_r)$ points. In the above equations, this can be seen from the fact that $\psi_1(k)$ is the envelope function multiplying an atomic density wave with wavevector k_r . We also note one particular higher-order effect that is not included in the above treatment. The missing effect arises from the fact that photon momentum must be conserved, $k^2 = k_\parallel^2 + k_\perp^2 = 4\pi^2/\lambda^2$. Consequently, phonons with nonzero k_\perp propagate in supermodes with a concomitantly reduced k_\parallel . Nevertheless, this effect is negligible for the momenta considered in the current experiment ($k_\perp/k_r \sim 10^{-2}$). For the largest momentum measured, the fractional change in the longitudinal momentum k_\parallel is less than 10^{-4} .

We also note that there should be a phonon dispersion in \hat{y} as well as that which we have shown in \hat{x} . We do not attempt to measure the dispersion in \hat{y} because we choose to make a BEC that is thin in this direction so as to maximise its length in \hat{x} . That is, the BEC is too thin in \hat{y} to support a full wavelength of the shortest-wavelength phonons we are able to stimulate at present.

IX. DERIVATION OF THE FORM OF THE LIGHT PROFILE EMITTED FROM THE CAVITY

We now derive the relationship of the intracavity field to that emitted by the cavity. Moreover, we describe how a phonon excitation at a particular momentum k_\perp appears in holographic images of the cavity field. We first show how each cavity field couples to momentum excitations. To do so, we consider the equation of motions in Eq. S24 and resolve $\hat{\psi}_1$ into the momentum basis

$$\hat{\psi}_1(\mathbf{r}) = \int d\mathbf{k} \hat{\psi}_{\mathbf{k}} e^{-i\mathbf{k} \cdot \mathbf{r}}. \quad (\text{S41})$$

The equations of motion for $\alpha_\mu \equiv \langle \hat{a}_\mu \rangle$ and $\beta_\mu \equiv \langle \hat{b}_\mu \rangle$ are

$$i\partial_t \alpha_\mu = -(\Delta_\mu + i\kappa)\alpha_\mu - \eta \int d\mathbf{k} \int d\mathbf{r} \Xi_\mu(\mathbf{r}) [\psi_0(\mathbf{r}) \psi_{\mathbf{k}}^* e^{i(\mathbf{k} \cdot \mathbf{r} + n_\mu \theta_0)} + \text{H.c.}], \quad (\text{S42})$$

$$i\partial_t \beta_\mu = -(\Delta_\mu + i\kappa)\beta_\mu - \eta \int d\mathbf{k} \int d\mathbf{r} \Xi_\mu(\mathbf{r}) [\psi_0(\mathbf{r}) \psi_{\mathbf{k}}^* e^{i(\mathbf{k} \cdot \mathbf{r} + n_\mu \theta_0)} + \text{H.c.}]. \quad (\text{S43})$$

We can consider the light profile due to the atomic population in a particular momentum mode $\psi_{\mathbf{k}}$. Focusing on the first degenerate resonance with even modes, and after setting the time derivative to zero, the light profile is

$$\begin{aligned} \tilde{\alpha}(\mathbf{r}, z) &= \sum_\mu \alpha_\mu \Xi_\mu(\mathbf{r}) \cos(k_r z - \theta_0 - \Theta - n_\mu \theta_0) \\ &= -\sum_\mu \eta \int d\mathbf{r}' \frac{\Xi_\mu(\mathbf{r}) \Xi_\mu(\mathbf{r}')}{\Delta_\mu + i\kappa} S_\mu^+ \psi_0(\mathbf{r}') \int d\mathbf{k} [\psi_{\mathbf{k}}^* e^{i(\mathbf{k} \cdot \mathbf{r}' + n_\mu \theta_0)} + \text{H.c.}] \cos(k_r z - \theta_0 - \Theta - n_\mu \theta_0), \end{aligned} \quad (\text{S44})$$

where the tilde signifies that this includes the profile along \hat{z} . Taking the forward-travelling part of the standing-wave intracavity field, we find the form of the cavity emission out of one of its cavity mirrors (for one of the two cavity fields):

$$\begin{aligned} \tilde{\alpha}^+(\mathbf{r}, z) &\propto e^{i(k_r z - \theta_0 - \Theta)} \sum_\mu \int d\mathbf{r}' \frac{\Xi_\mu(\mathbf{r}) \Xi_\mu(\mathbf{r}')}{\Delta_\mu + i\kappa} S_\mu^+ \psi_0(\mathbf{r}') \int d\mathbf{k} [\psi_{\mathbf{k}}^* e^{i\mathbf{k} \cdot \mathbf{r}'} + \psi_{\mathbf{k}} e^{-i(\mathbf{k} \cdot \mathbf{r}' + 2n_\mu \theta_0)}] \\ &\propto e^{i(k_r z - \theta_0 - \Theta)} \int d\mathbf{k} \int d\mathbf{r}' \psi_0(\mathbf{r}') \left[\mathcal{G}^+(\mathbf{r}, \mathbf{r}', 0) \psi_{\mathbf{k}}^* e^{i\mathbf{k} \cdot \mathbf{r}'} + \mathcal{G}^+(\mathbf{r}, \mathbf{r}', -2i\theta_0) \psi_{\mathbf{k}} e^{-i\mathbf{k} \cdot \mathbf{r}'} \right], \end{aligned} \quad (\text{S45})$$

where $\mathcal{G}^+(\mathbf{r}, \mathbf{r}', \varphi)$ is a modified Green's function defined as [26]

$$\begin{aligned} \mathcal{G}^+(\mathbf{r}, \mathbf{r}', \varphi) &= \mathcal{G}(\mathbf{r}, \mathbf{r}', \varphi) + \mathcal{G}(\mathbf{r}, -\mathbf{r}', \varphi), \\ \mathcal{G}(\mathbf{r}, \mathbf{r}', \varphi) &= \sum_\mu \frac{\Xi_\mu(\mathbf{r}) \Xi_\mu(\mathbf{r}') e^{-n_\mu \varphi}}{1 + \tilde{\epsilon} n_\mu + i\tilde{\kappa}}. \end{aligned} \quad (\text{S46})$$

The calculation for β_μ proceeds in the same way, with the only difference being the aforementioned additional $\pi/2$ phase shift:

$$\begin{aligned}\tilde{\beta}(\mathbf{r}, z) &= \sum_{\mu} \beta_{\mu} \Xi_{\mu}(\mathbf{r}) \sin(k_r z - \theta_0 - \Theta - n_{\mu} \theta_0) \\ &= - \sum_{\mu} \eta \int d\mathbf{r}' \frac{\Xi_{\mu}(\mathbf{r}) \Xi_{\mu}(\mathbf{r}')}{\Delta_{\mu} + i\kappa} \psi_0(\mathbf{r}') \int d\mathbf{k} [i\psi_{\mathbf{k}}^* e^{i(\mathbf{k} \cdot \mathbf{r}' + n_{\mu} \theta_0)} + \text{H.c.}] \sin(k_r z - \theta_0 - \Theta - n_{\mu} \theta_0),\end{aligned}\quad (\text{S47})$$

$$\begin{aligned}\tilde{\beta}^+(\mathbf{r}, z) &\propto e^{i(k_r z - \theta_0 - \Theta)} \sum_{\mu} \int d\mathbf{r}' \frac{\Xi_{\mu}(\mathbf{r}) \Xi_{\mu}(\mathbf{r}')}{\Delta_{\mu} + i\kappa} \psi_0(\mathbf{r}') \int d\mathbf{k} [\psi_{\mathbf{k}}^* e^{i\mathbf{k} \cdot \mathbf{r}'} - \psi_{\mathbf{k}} e^{-i(\mathbf{k} \cdot \mathbf{r}' + 2n_{\mu} \theta_0)}] \\ &\propto e^{i(k_r z - \theta_0 - \Theta)} \int d\mathbf{k} \int d\mathbf{r}' \psi_0(\mathbf{r}') \left[\mathcal{G}^+(\mathbf{r}, \mathbf{r}', 0) \psi_{\mathbf{k}}^* e^{i\mathbf{k} \cdot \mathbf{r}'} - \mathcal{G}^+(\mathbf{r}, \mathbf{r}', -2i\theta_0) \psi_{\mathbf{k}} e^{-i\mathbf{k} \cdot \mathbf{r}'} \right].\end{aligned}\quad (\text{S48})$$

After measuring the cavity field emission from both frequencies, the total field can be reconstructed digitally by summing Eqs. S45 and S48:

$$\Phi(\mathbf{r}) \propto \int d\mathbf{k} \int d\mathbf{r}' \psi_0(\mathbf{r}') \mathcal{G}^+(\mathbf{r}, \mathbf{r}', 0) \psi_{\mathbf{k}}^* e^{i\mathbf{k} \cdot \mathbf{r}'}.\quad (\text{S49})$$

Therefore, the digitally summed image contains the contribution from only the local part $\mathcal{G}(\mathbf{r}, \mathbf{r}', 0)$ of the field because the nonlocal contribution from $\mathcal{G}(\mathbf{r}, \mathbf{r}', -2i\theta_0)$ cancels, as shown in Fig. 2 in the main text.

In the limit of an ideal confocal cavity in which $\mathcal{G}(\mathbf{r}, \mathbf{r}', 0)$ becomes a δ -function (i.e., perfect mode degeneracy), Eq. (S49) shows that a single momentum component $\psi_{\mathbf{k}}$ will result in a phase winding $e^{i\mathbf{P} \cdot \mathbf{r}}$ on the reconstructed cavity emission. Taking the Fourier transform of the complex electric field $\Phi(\mathbf{r})$ then reveals the momentum mode that has been stimulated through Bragg spectroscopy. Furthermore, this also shows that a particular momentum can be excited by stimulating the local part of the field and probing on either one of the degenerate resonances.

Though we do not employ this here, we note that the nonlocal part of the cavity emission—i.e., the part that could be found by digitally subtracting the images at the two cavity frequencies—also provides information about the driven momentum. This is because, for a confocal cavity with a BEC confined to the cavity midpoint $z = 0$, this emission is the Fourier transform of the object image. Consider the simple case of an ideal confocal cavity with atoms located at the midplane of the cavity where $\theta_0 = \pi/4$. The nonlocal part of the emitted field is

$$\begin{aligned}\Phi_{\text{nonlocal}}(\mathbf{r}) &\propto \int d\mathbf{k} \int d\mathbf{r}' \psi_0(\mathbf{r}') \cos\left[\frac{2\mathbf{r} \cdot \mathbf{r}'}{w_0^2}\right] \psi_{\mathbf{k}}^* e^{i\mathbf{k} \cdot \mathbf{r}'} \\ &= \frac{1}{2} \int d\mathbf{k} \int d\mathbf{r}' \psi_0(\mathbf{r}') \psi_{\mathbf{k}}^* \left\{ \exp\left[i\left(\mathbf{k} + \frac{2\mathbf{r}}{w_0^2}\right) \cdot \mathbf{r}'\right] + \exp\left[i\left(\mathbf{k} - \frac{2\mathbf{r}}{w_0^2}\right) \cdot \mathbf{r}'\right] \right\},\end{aligned}\quad (\text{S50})$$

which contains direct information about the excited momentum modes $\psi_{\mathbf{k}}$.

X. COUPLING OF A LONGITUDINAL PROBE FIELD INTO THE CONFOCAL CAVITY

The Hamiltonian for a longitudinally driven multimode cavity is given by

$$H = - \sum_{\mu} [\Delta_{\mu} \hat{a}_{\mu}^{\dagger} \hat{a}_{\mu} + f_{\mu} (\hat{a}_{\mu} + \hat{a}_{\mu}^{\dagger})],\quad (\text{S51})$$

where

$$f_{\mu} = \int d\mathbf{r}' f(\mathbf{r}') \Phi_{\mu}(\mathbf{r}', z_0)\quad (\text{S52})$$

is the spatial overlap between the longitudinal pump $f(\mathbf{r})$ and a cavity mode $\Phi_{\mu}(\mathbf{r}, z)$ near a particular plane $z = z_0$ is

$$\Phi_{\mu}(\mathbf{r}, z_0) = \Xi_{\mu}(\mathbf{r}) \cos[k_r z_0 - \theta_{\mu}(z_0)].\quad (\text{S53})$$

Ignoring cavity loss, the classical equation of motion of the expectation value $\alpha_{\mu} = \langle \hat{a}_{\mu} \rangle$ is

$$i\partial_t \alpha_{\mu} = \Delta_{\mu} \alpha_{\mu} + f_{\mu}.\quad (\text{S54})$$

In steady state, the total transverse light field is therefore given by

$$\alpha(\mathbf{r}) = \sum_{\mu} \alpha_{\mu} \Phi_{\mu}(\mathbf{r}, z_0) = \sum_{\mu} \frac{f_{\mu} \Phi_{\mu}(\mathbf{r}, z_0)}{\Delta_{\mu}}. \quad (\text{S55})$$

Focusing on the transverse profile, the cavity field is

$$\alpha(\mathbf{r}) = \int d\mathbf{r}' f(\mathbf{r}') \sum_{\mu} \frac{\Xi_{\mu}(\mathbf{r}) \Xi_{\mu}(\mathbf{r}') \cos^2[k_r z_0 - \theta_{\mu}(z_0)]}{\Delta_{\mu}} \mathcal{S}_{\mu}^{+} \equiv \int d\mathbf{r}' f(\mathbf{r}') \mathcal{T}(\mathbf{r}, \mathbf{r}'), \quad (\text{S56})$$

where θ_{μ} is the longitudinal phase of mode μ at the transverse plane $z = z_0$ we are considering. The factor \mathcal{S}_{μ}^{+} restricts the summation to modes with even transverse spatial symmetry for the case of a degenerate resonance in a confocal cavity. Thus, the transfer function \mathcal{T} for an longitudinally input beam profile can be evaluated the same way as the Green's function for the cavity-mediated interaction.

In an ideal confocal cavity, at the cavity midplane, the transfer function contains three parts [26]:

$$\mathcal{T}(\mathbf{r}, \mathbf{r}') \propto \delta\left(\frac{\mathbf{r} - \mathbf{r}'}{w_0/\sqrt{2}}\right) + \delta\left(\frac{\mathbf{r} + \mathbf{r}'}{w_0/\sqrt{2}}\right) + \frac{1}{\pi} \cos\left(\frac{2\mathbf{r} \cdot \mathbf{r}'}{w_0^2}\right). \quad (\text{S57})$$

For a longitudinal probe profile localised around the atoms, the resulting cavity field will contain the probe field, its mirror image, and a nonlocal contribution. In a realistic cavity where the transverse modes are not fully degenerate (such as ours), the highest spatial-frequency components of the input probe field will be suppressed.

XI. COMPARISON TO OTHER SYSTEMS

In a crystallisation transition, the mutual interactions of the particles in a gas or liquid conspire to break a continuous translational $U(1)$ symmetry. While the periodicity of the resultant lattice is set by properties of the particles themselves, the phase of the lattice freely emerges. Goldstone's theorem implies that after solidification, the lattice may, in principle, slide at no energy cost since no particular phase had been preferred [44]. While this zero-momentum ($k = 0$) mode contributes nothing to the thermodynamic properties of the solid, long-wavelength (small k) phonon modes that do contribute also arise from the broken symmetry. These connect with the $k = 0$ mode to form a continuous, gapless spectrum of excitations called a Goldstone mode.

While the amplitude of the lattice is emergent in a single-mode, single-pumped cavity, its phase and periodicity are geometrically fixed by the single cavity mode into which the photons scatter—the lattice remains inelastic. Adding a second, frequency-degenerate cavity mode creates a standing-wave potential for the atoms with an emergent phase, thereby breaking the $U(1)$ symmetry. As the atoms move, so does the standing wave, realising the $k = 0$ point of a Goldstone mode. Such a scheme was experimentally realized using two crossed single-mode Fabry-Pérot cavities tuned to the same frequency [22]. Pumped atoms scatter photons into a superposition of the two modes. Their coherent sum yields a $U(1)$ phase degree of freedom and realises a lattice with the same $k = 0$ mode mentioned above. With the atoms Bose-condensed, a simple supersolid is created wherein superfluidity and periodic structure arising from the broken translational symmetry coexist. Absent, however, are phonons. This is because the infinite-range, photon-mediated interactions of each single-mode cavity yield an effectively 0D system with no $k > 0$ modes [23, 45]—the Goldstone dispersion is missing. A similar $k = 0$ Goldstone mode of a dipolar supersolid has been observed [46].